The Role of Noise in Ocean Circulation Variability Applications of the Dynamical Orthogonal Field Method

C.E.Wieners

November 13, 2013

Abstract

Short-time fluctuations in oceanic systems which cannot be resolved in models but might have influence on larger-scale phenomena, can be incorporated als stochastic (white or red) noise. However, this requires solving stochastic partial differential equations, which means that one has to perform calculations for a large number of realisations. The Dynamically Orthogonal (DO) field method has been developed to deal with such systems in an efficient way, namely by decomposing the realisations $\psi(\omega)$ into a mean $\bar{\psi}$ and modes ψ_i as

$$\psi(\omega) = \bar{\psi} + \sum_{i=1}^{N_{mode}} \psi_i Y_i(\omega)$$

where $Y_i(\omega)$ are (stochastic) coefficients, and then considering only the most dominant modes of variability. The modes have to be kept orthogonal by means of a projection in each time step [Sapsis, Lermusiaux 2009].

In this master project, the DO method is applied to two oceanic systems, the Kuroshio-current (wind-driven circulation) and El Niño.

The Kuroshio-current can be simulated in a (rather simplistic) Double Gyre system on the βplane. The governing equations, basin geometry and boundary conditions all have a mirror symmetry for North-South reflection against the middle line of the basin. For low Reynolds numbers, solutions are symmetric, but the symmetric state becomes unstable at $Re = 30$ (pitchfork bifurcation). This is believed to explain the bimodal behaviour of the Kuroshio-current. The stable branches of the pitchfork become unstable at $Re = 53$ because of a Hopf bifurcation [Dijkstra,Katsman 1997].

For the Double Gyre system a DO-computer code already existed and parts of the parameter space (low Reynolds number) were already investigated [Sapsis, Dijkstra 2013]. The main focus in this project lies on the region between the pitchfork bifurcation and the first Hopf bfurcation which destabilises the pitchfork branches.

It turned out that the mean is a more or less symmetric state and the first mode describes the difference between the pitchfork branches and the mean. Other modes describe transient deviations from these pitchfork branches. In particular, one finds a Gyre mode, which is associated to the second Hopf bifurcation at $Re \approx 80$, with a period of about one year, and Rossby basin modes, associated with the first Hopf bifurcation, which have a period of about 2 months. The latter seems to show coherence resonance behaviour, being excited more easily the closer one comes to the Hopf bifurcation, while the former can even be excited at rather low Reynolds numbers $Re = 42$.

For El Niño the DO equations had to be derived and implemented them into an existing (DO-free) code for the Zebiak-Cane model of El Niño. In particular, an inner product for the orthogonality projection had to be defined. It turned out that in case of a non-trivial inner product, the procedure for obtaining the initial conditions as described in [Sapsis, Lermusiaux 2009] has to be generalised. Also the question arose whether it is consistent to take the co-called long-wave limit (neglecting the time derivative in the meridional momentum equation) before or after applying the DO method; these two procedures are indeed equivalent.

Unfortunately, time was running out before the code run reliably, but a few preliminary studies with the original code suggest that the Zebiak-Cane equations contain a Hopf bifurcation in the parameter governing the heating of the atmosphere by the ocean. Variability before this bifurcation increases significantly when applying noise - especially red noise -, and the empirical orthogonal functions associated with this variability indeed resemble El Niño. This suggests that El Niño might be described as a system before the Hopf bifurcation, which can be excited by noise.

Contents

1 Introduction

1.1 Noise in Ocean Models

Even though the governing equations of fluid flow are known, it is impossible to resolve all phenomena in ocean models. This is due to the enormous range of scales - from ocean currents extending over thousands of kilometers and with time scales of months or years down to turbulence at a scale of centimeters and seconds. It is not possible to cover an ocean basin of thousand kilometers width with a grid with a cell length of a centimeter, or to run a model over thousand years with time steps of a second. Also, when dealing with large-scale phenomena, one is usually not interested in the details of small-scale processes. The only thing that matters is their influence on the large-scale phenomenon.

An interesting way to incorporate short timescale processes without actually resolving them is to implement them as stochastic noise. This is actually not correct - for example, synoptic-scale fenomena are predicted daily in the weather forecast, so they are not stochastic. Yet from the point of view of slow processes, like climate changes or ocean dynamics, the atmosphere undergoes some rapid changes of which the underlying mechanisms are not relevant for the slow process. So one can just as well describe the fast process as noise.

In this thesis, I will deal with two ocean-atmosphere systems, the wind-driven circulation and El Niño. In both cases it will be the atmosphere which is responsible for the noise. Even though it is partially governed by long timescale processes such as the global circulation or (in case of ENSO) coupling to the ocean surface temperature, the atmosphere can exhibit short-time phenomena such as high- and low pressure areas. The ocean is more inert because of its higher heat capacity and slower velocities.

Including noise means that instead of deterministic partial differential equations we have to solve stochastic partial differential equations (SPDE's). One method to deal with them is the Dynamically Orthogonal Field (DO) method, which yields both the most dominant patterns (modes) of variance and probability density functions associated to these modes.

1.2 Choice of the example systems

1.2.1 The Kuroshio currrent (Double Gyre System)

The Kuroshio current is part of the wind-driven circulation in the Northwestern Pacific ocean; a westward current near Japan which forms the northern branch of the subtropical gyre (clockwise circulation driven by the winds around the subtropical high pressure area) and the southern branch of the -rather deformed- counterclockwise subpolar gyre. In this thesis the double gyre will be treated as a purely wind-driven circulation; density effects are ignored.

The Kuroshio current shows a bimodial behaviour; it switches from the 'small meander state' to the 'large meander state' (see fig. 1) once in a few years. On top of that, it also displays fluctuation on shorter (intermonthly) timescales, such as the 7monthly fluctuation in fig. 1 which is caused by Rossby basin modes (Rossby waves in a bounded basin, i.e. obeying boundary conditions). The double gyre system can be described with a comparatively simple set of equations, which nevertheless capture both features. The bimodal behaviour is associated to a pitchfork bifurcation at Reynolds number $Re \approx 30$, whereas intermonthly oscillations are associated with Hopf bifurcations. [Dijkstra 2005].

Apart from the climatologic winds which cause the gyre, there are strong short-time fluctuations - noise - , for example due to mid-latitude cyclones. The effect of this atmospheric noise on the variability of the gyre can be studied using the DO method. Some studies at low Reynolds number have already been performed[Sapsis, Dijkstra 2013] and a computer code also exists. The focus in this thesis lies on the behaviour before the first Hopf bifurcation, in particular on the question whether - and how - it is possible to excite Hopf modes by noise before actually reaching the bifurcation (coherence resonance). Apart from being interesting in itself, studying the double gyre might also be usefull preliminary work for the more complex ENSO (El Niño - Southern Oscillation) system, which also has a Hopf bifurcation.

1.2.2 El Niño

El Niño's (major warm water anomalies in the eastern equatorial Pacific) occur with a preferred frequency of $1/(3-4 years)$, but in a very irregular manner (see fig. 2). The order of magnitude of the recurrence time is given by oceanic quantities which are inherent to the system: the time it takes for a Kelvin wave (carrying the warm/cold signal of a beginning El Niño/La Niña) to cross the Pacific ocean and to be reflected at the eastern coast into Rossby waves which then travel back.

But the irregularity is harder to explain. There are two possible explanations [Kleeman 2010]:

1. The 'optimist's view': The system has strong couplings and is sufficiently non-linear that the slow modes interact in a chaotic manner. If we are smart enough to unravel the dynamics, we can predict El Niño.

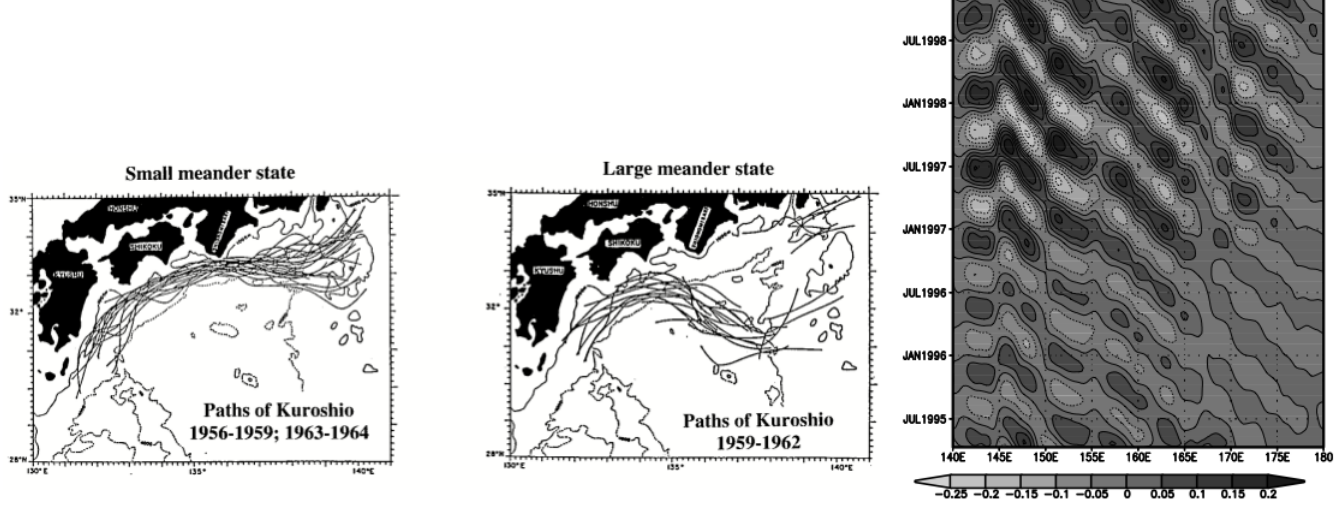

Figure 1: Left and middle panel: Paths of the Kuroshio current in its small (left) and large (middle) meander state. Taken from [Schmeits, Dijkstra 2001].
Right panel: Hovmoller diagram of the sea surface height anomaly (in m) associated with a Rossby basin mode along 35^{o}North. The period is 7 months. Taken from [Schmeits, Dijkstra 2002]

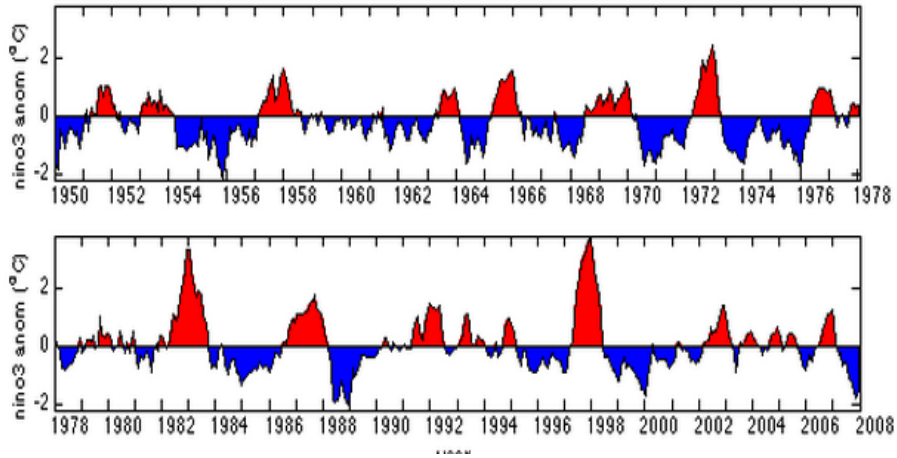

Figure 2: Timeseries of the sea surface at the Nino3 region. Positive anomalies correspond to El Niño.

2. The 'pessimist's view': The system might be rather weakly-coupled and is mainly noise-driven. Atmospheric effects, like the Madden-Julian oscillation, might be needed to trigger El Niño's. The predictability of a noise-driven system is naturally limited.

Mathematically speaking, there is a Hopf bifurcation in the heating parameter which couples the sea surface temperature to its response in the atmosphere. In case of the 'optimist's explanation', the system is past the Hopf bifurcation and oscillates without external input; in the second case, it is just before the Hopf and Hopf-like modes can be excited by noise forcing.

El Niño has not been studied with the DO method before. Within this project I derived the DO equations for El Niño and implemented them into an existing version of a code of the Zebiak-Cane (ZC) model [Zebiak, Cane 1987], a comparatively simple model capturing the main features of El Niño. Unfortunately, there was not enough time to finish the computer code for ENSO. However, a few preliminary studies were performed with the original ZC model which suggest that the Hopf-like modes can indeed be triggered by noise.

2 Dynamically Orthogonal Field Method

When working with stochastic noise, one is interested in stochastic properties of the system, like mean states or modes of variability or probability density functions (pdf's). This means that one has to perform computations for a whole ensemble of realisations. However, this takes a lot of computation time and is therefore not practicable.

But it is often observed that most of the variance of a stochastic system comes from only a few dominant modes. Together with the mean, they capture most of the features of the system. The DO method is based on only considering the dominant N_{mode} modes and decomposing the realisations according to

$$\varphi(x,t,\omega) = \bar{\varphi}(x,t) + \sum_{i=1}^{N_{mode}} Y_i(t,\omega)\varphi_i(x,t)$$

where ω denotes the realisation, φ_i the modes, and $\bar{\varphi}$ the mean. The $Y_i(\omega)$ are called stochastic coefficients.

Instead of computing the time evolution of a large number of realisations, one only has to solve (deterministic) PDE's for the mean and the modes, and stochastic ODE's for the coefficients.

I will now briefly describe the DO formalism, following [Sapsis, Lermusiaux 2009].

2.1 Stochastic Partial Differential Equations (SPDE)

A general stochastic partial differential equation is of the form

$$\frac{\partial\varphi(x,t,\omega)}{\partial t} = \widetilde{\mathcal{L}}[\varphi(x,t,\omega),\omega] \tag{1}$$

where φ denotes the fields, ω a realisation from probability space Ω, $\widetilde{\mathcal{L}}$ a (spatial) differential operator which in general depends on the stochastic event.

In our case $\widetilde{\mathcal{L}}$ can be written as $\mathcal{L}[\varphi(x,t,\omega)] + F(x,t,\omega)$, that is, it can be decomposed into deterministic part plus a stochastic (white or red noise) forcing.
The initial condition is given by

$$\varphi(x,t_0,\omega) = \varphi_0(x,\omega) \tag{2}$$

and the boundary condition

$$\mathcal{B}[\varphi(y,t,\omega)] = h(y,t,\omega) \quad y \in \partial D \tag{3}$$

where $\mathcal{B}$ is a linear differential operator and D the domain, so ∂D is the boundary of the domain.

2.2 Definitions

Notation The Einstein sum convention will be applied for double indices, i.e. $\sum_i a_i b_i$ will be written as $a_i b_i$. If no summation is intended, this is indicated by a bar on top of the indices, $a_{\bar{i}} b_{\bar{i}}$.
Greek letters like φ, χ can denote a whole vector of fields, such as $\varphi = (u,v,p)^T$, where the superscript ^{T} indicates a transition from row to column vector.

Mean Value Operator The mean over stochastic space of any quantity, like, for example, the vector φ, is calculated like this:

$$\bar{\varphi}(x,t) = E^{\omega}[\varphi(x,t,\omega)] = \int_{\Omega} \varphi(x,t,\omega) d\mathcal{P}(\omega) \tag{4}$$

where ω denotes the realisation, Ω the space of all realisations, and $\mathcal{P}(\omega)$ a probability measure.

The deviation from the mean is given by $\widetilde{\varphi}(x,t,\omega) \equiv \varphi(x,t,\omega) - \bar{\varphi}(x,t)$.

Spatial Inner Product The spatial inner product is given by

$$< \varphi(.,t,\omega), \chi(.,t,\omega) >= \int_D \varphi_a(x,t,\omega) A_{ab} \chi_b(x,t,\omega) dx \tag{5}$$

where the latin indices denote field components (remember, φ is in general a vector of several fields) and A_{ab} , the inner product metric, is a positive symmetric matrix. A natural choice is to make the scalar product proportional to the energy of the system - it is positive definite, inherent to the system, and conserved. The exact form of the metric will be discussed for each system below.

Covariance Operator In [Sapsis, Lermusiaux 2009], the following definition is used for the Covariance operator:

$$C_{\varphi(.,t,\omega),\chi(.,t,\omega)}(x,y) = E^{\omega}[\widetilde{\varphi}(x,t,\omega) \otimes_{ab} \widetilde{\chi}(y,t,\omega)] \tag{6}$$

It will turn out that in case of a non-trivial metric (not a multiple of the unity matrix) this definition should be generalised (see part4.3.3).
The symbol $\otimes_{ab}$ denotes the tensor product[1] in the field component space; for example, if $\varphi = (u,v,p)^T$ then a, b stand for u, v or p.
The fields which obey $\int_{\omega}[\varphi^T(x,t,\omega), \varphi(x,t,\omega)]dx < \infty$ form a Hilbert space with C_{φ} as bilinear form.

2.3 DO Decomposition and Equations

Decomposition Any stochtasic φ-field of the Hilbert space can be decomposed as

$$\varphi(x,t,\omega) = \bar{\varphi}(x,t) + \sum_{i=1}^{\infty} Y_i(t,\omega)\varphi_i(x,t) \tag{7}$$

where $Y_i(t,\omega)$ are zero-mean and the φ_i obey

$$\int_D C_{\varphi(.,t,\omega),(.,t,\omega)}(x,y)\varphi_i(x,t,\omega)dx = \lambda_i^2(t)\varphi_{\bar{i}}(y,t) \tag{8}$$

In eq.7 φ can be arbitrarily well approximated using a finite[2], but sufficiently large, number of modes (N_{mode}), associated with the N_{mode} largest eigenvalues:

$$\varphi(x,t,\omega) = \bar{\varphi}(x,t) + \sum_{i=1}^{N_{mode}} Y_i(t,\omega)\varphi_i(x,t) \tag{9}$$

One defines $V_s = \{\varphi_i(x,t)\}_{i=1}^{N_{mode}}$ - it is the space of the modes which are considered in the approximation of φ.

Eq. 9 contains a redundancy because if the $\varphi_i(x,t)$ change in time in such a way that the change is in the span of the $\varphi_i(x,t)$, i.e. in V_s, then one could have achieved the same change in φ by just varying the $Y_i(t,\omega)$. Hence one imposes $\frac{dV_s}{dt} \perp V_s$ which implies

$$< \varphi_i(.,t), \frac{\partial \varphi_j}{\partial t}(.,t) >= 0 \tag{10}$$

This also ensures that the modes remain orthogonal to each other [Sapsis, Lermusiaux 2009].

Equations Notation:

The generalised (more than two variables) covariance matrix between two or more modes is defined by

$$C_{ijk...} = E^{\omega}[Y_iY_jY_k...]$$

In particular, C_{ij} is a matrix in the space of DO-modes: $C_{ij} = E^{\omega}[Y_iY_j]$; this two-variable case will simply called the covariance matrix.

It will also be handy to define the projection operator,

$$\Pi_{v_s^{\perp}}[\chi(x)] = \chi(x) - < \chi(\bullet), \varphi_k(\bullet,t) > \varphi_k(x)$$

which projects a vector χ onto the space perpendicular to all DO-modes φ_k.

The mean flow, modes and stochstic coefficients Y_i evolve according to the following evolution equations:

$$\frac{dY_i(t,\omega)}{dt} =< \widetilde{\mathcal{L}}[\varphi(\bullet,t,\omega);\omega] - E^{\omega}[\widetilde{\mathcal{L}}[\varphi(\bullet,t,\omega);\omega]], \varphi_i(\bullet,t) > \tag{11}$$

$$\partial_t\bar{\varphi} = E^{\omega}[\widetilde{\mathcal{L}}[\varphi(\bullet,t,\omega);\omega]] \tag{12}$$

[1] the tensor product of two vectors is given by $a \otimes b = \begin{pmatrix} a_1b_1 & a_1b_2 & ... \\ a_2b_1 & a_2b_2 & ... \\ ... & ... & ... \end{pmatrix}$ or $a\,b^T$.

[2] in case of discretised fields, the number of possible modes is finite anyway, but far larger than the number of modes one wants or needs to consider in the DO method.

$$\partial_t \varphi_i = \Pi_{v_s^\perp}[E^\omega[\widetilde{\mathcal{L}}[\varphi(\bullet,t,\omega);\omega]Y_i(t,\omega)]]C^{-1}_{i,j} \tag{13}$$

Note that the mean flow and the DO-modes are deterministic, i.e. they do not depend on the stochastic variable ω. The stochasticity of φ lies entirely in the stochastic coefficients, Y_i, which follow from ODE's. Hence one has to solve $N_{mode}+1$ deterministic PDE's and N_{mode} stochastic ODE's.

The boundary conditions become

$$\mathcal{B}[\bar{\varphi}(y,t)]|_{y\in\partial D} = E^\omega[h(y,t,\omega)] \tag{14}$$

$$\mathcal{B}[\varphi_i(y,t)]|_{y\in\partial D} = E^\omega[h(y,t,\omega)Y_i(t,\omega)]C^{-1}_{i,j} \tag{15}$$

and the initial conditions are

$$Y_i(t_0,\omega) =< \widetilde{\varphi}_0(\bullet,\omega), \varphi_{0i}(\bullet) > \tag{16}$$

where still $\widetilde{\varphi} \equiv \varphi - \bar{\varphi}$.

$$\bar{\varphi}(x,t_0) = \bar{\varphi_0}(\bullet) \equiv E^\omega[\varphi_0(x,\omega)] \tag{17}$$

$$\varphi_i(x,t_0) = \varphi_{i0}(x) \tag{18}$$

where φ_{i0} are the eigenfields of the covariance operator, $C_{\varphi(\bullet,t_0),\varphi(\bullet,t_0)}$. Note that at later times the DO-modes neend't be eigenmodes of the correlation operator anymore.

3 Wind-driven Circulation: Double Gyre System

3.1 The Double Gyre System

3.1.1 System Equations

The derivation of the model equation is only sketched very roughly here. For details, I refer to [Dijkstra 2005].

For the double gyre system, we assume constant water density and apply the β-plane approximation, that is, we assume limited meridional extend and use Cartesian coordinates, but include the meridional variation of the Coriolis parameter up to first order in Taylor expansion: $f = f_0 + \beta_0 y$. With these approximations one obtains the following non-dimensional equations (parameters are listed in table 1):

$$\epsilon D_t u - v(1+\beta\epsilon y) + \partial_x p = E_H[\partial_x^2 u + \partial_y^2 u] + E_V[\partial_z^2 u] \tag{19}$$

$$\epsilon D_t v + u(1+\beta\epsilon y) + \partial_y p = E_H[\partial_x^2 v + \partial_y^2 v] + E_V[\partial_z^2 v] \tag{20}$$

$$\partial_z p = 0 \tag{21}$$

$$\partial_x u + \partial_y v + \partial_z w = 0 \tag{22}$$

For brevity ∂_x denotes the partial derivative $\frac{\partial}{\partial x}$, and D_t the total time derivative $D_t = \partial_t + u\partial_x + v\partial_y + w\partial_z$.
Note that p denotes the dynamic (and dimensionless) pressure, that is, the hydrostatic component due to the depth below the average sea surface is substracted from the physical pressure ($p_{phys} = \rho_0 U f_0 L p - \rho_0 g D z$ where $z=0$ at the surface and $z=-1$ at the bottom, and p_{phys} is the dimensionfull pressure). The pressure depends now only on the (dimensionless) surface height η:

$$p = \epsilon\, Fr\, \eta \tag{23}$$

There is one more boundary condition at the surface, namely continuity of stress:

$$E_V\partial_z u = \alpha_{SW}\tau^x \ , \ E_V\partial_z v = \alpha_{SW}\tau^y \tag{24}$$

where (τ^x,τ^y) denotes the wind stress,
while at the bottom, there is no flow through the sea floor (height η_b), i.e. a fluid element on the boundary remains there:

parameter	explanation	composed parameter	formula
U	typical horiz. velocity	ϵ (Rossby number)	U/f_0L
L	typical horizontal length scale	Fr (Froude number)	gD/U^2
D	Depth	α_{SW}	$\tau_0/(f_0\rho_0 DU)$
τ_0	typical wind stress scale	E_H (horizontal Ekman number)	A_H/f_0L^2
A_H, A_V	horiz./vert. friction coefficient	E_V (horizontal Ekman number)	A_V/f_0D^2
f_0	Coriolis parameter	Re (Reynolds number)	$E_H/\epsilon = UL/A_H$
β_0	beta parameter (dimensional)	α_{QG}	$\tau_0 L/\rho_0 DU^2$
		r_b (bottom friction parameter)	$\sqrt{E_V/\epsilon}$
		F (rotational Froude number)	$f_0^2L^2/gD$
		β (dimensionless beta parameter)	$\beta = \beta_0 \frac{L^2}{U}$

Table 1: List of the parameters used in the Double Gyre model

$$D_t(z - \eta_b) = 0 \tag{25}$$

Assuming small Ekman numbers E_V, E_H and small Rossby number ϵ, one can do an expansion in ϵ:

$$\chi = \chi_0 + \epsilon\chi_1 + \epsilon^2\chi_2 ...; \;\; \chi = u, v, p, ...$$

and obtains that to zeroth order, the velocities are depth-independent:

$$u_0 = -\partial_y p \;, \;\; v_0 = \partial_x p$$

However, this means that the boundary conditions cannot be satisfied. Near the upper and lower boundary, however, the typical vertical scale is smaller, so ∂_z^2 terms become large there. So while in the bulk of the ocean the system is, to zeroth order, in geostrophic equilibrium, one needs to include the $E_V\partial_z^2\mathbf{u}$ terms ($\mathbf{u} = (u, v)$) in the top and bottom layers (Ekman layers). This makes it possible to simplify the equations by performing vertical integration and using the results of the Ekman dynamics for the boundary conditions:

$$\epsilon\tilde{D}_t u - (1 + \beta\epsilon y)v = -\epsilon\, Fr\, \partial_x h + E_H\nabla^2 u + \alpha_{SW}\tau^x/h \tag{26}$$

$$\epsilon\tilde{D}_t v + (1 + \beta\epsilon y)u = -\epsilon\, Fr\, \partial_y h + E_H\nabla^2 v + \alpha_{SW}\tau^y/h \tag{27}$$

$$\partial_t h + \partial_x(hu) + \partial_y(hv) = 0 \tag{28}$$

with the two-dimensional total time derivative $\tilde{D}_t = \partial_t + u\partial_x + v\partial_y$. (From now on, the tilde will be omitted while describing gyres, because only a two-dimensional set of equations will be used.) h denotes the ocean depth, including bottom topography and surface deviation. u, v are now depth-averaged velocities.

In the case of small Rossby number and small bottom topography ($\eta_b = \mathcal{O}(\epsilon)$), the equations can be simplified further still. Using the same expansion as above, one finds

$$u_0 = -\partial_y p_0 \equiv -\partial_y\psi \;, \;\; v_0 = \partial_x p_0 \equiv \partial_x\psi$$

where ψ is the stream function. Denoting by ζ the vorticity,

$$\zeta = \partial_x v - \partial_y u = \nabla^2\psi$$

then one can eliminate the pressure by taking ∂_y(eq. 27)-∂_x(eq. 27) and obtains to first order in ϵ the quasi-geostrophic vorticity equation:

$$D_t[\zeta - F\psi + \beta y] = 1/Re\;\nabla^2\zeta - r_b\nabla^2\psi + \alpha_{QG}(\partial_x\tau^y - \partial_y\tau^x) \quad , \; \zeta = \nabla^2\psi \tag{29}$$

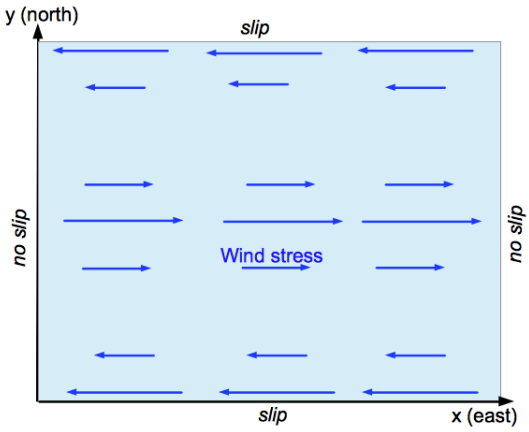

Figure 3: Domain and wind forcing of the gyre system: The basin is rectangular, with no-slip boundary conditions at the meridional sides and no-slip conditions at the zonal boundaries. The wind forcing, indicated by blue arrows, is zonal and has a sinusoidal y-dependence.

3.1.2 Symmetry and Bifurcation Diagram

In this project, eq. 29 is solved in a very idealised domain, namely a quadratic basin ($L_x = L_y = 1$ in non-dimensional quantities) with constant depth. No flow is allowed through the boundaries:

$$u(0,y) = u(1,y) = 0 \ , \ v(x,0) = v(x,1) = 0 \tag{30}$$

No-slip conditions are assumed along the western and eastern boundaries, where the ocean bounded by continents, and slip conditiond at the northern and southern boundaries, where basin is open to the rest of the ocean:

$$v(0,y) = v(1,y) = 0 \ , \ \partial_x u(x,0) = \partial_y u(x,1) = 0 \tag{31}$$

This can be summarised in terms of the stream function:

$$\psi(0,y) = 0 \ , \ \partial_x \psi = 0 \ , \ \ (x = 0,1) \tag{32}$$

$$\psi = 0 \ , \ \partial_y^2 \psi = 0 \ , \ (y = 0,1) \tag{33}$$

The deterministic wind forcing is idealised, too; we assume zero meridional (north-south) wind and sinusoidal zonal wind: $\tau^x = -\tau^0 \cos(2\pi y) \ , \ \tau^y = 0$.

With this wind forcing, basin geometry and boundary conditions, the eq. 29 is symmetric with respect to reflection about the line $y = 1/2$. It is interesting to see whether the solutions also have this symmetry $\mathcal{R}$:

$$\mathcal{R}(\psi(x,1-y)) = -\psi(x,y) \tag{34}$$

which manifests itself in the velocity field as

$$\mathcal{R}(u(x,1-y)) = u(x,y) \ , \ \mathcal{R}(v(x,1-y)) = -v(x,y)$$

Dijkstra and Katsman performed an analysis of the bifurcation diagram of the system, using a pseudo-arclength continuation method [Dijkstra,Katsman 1997]. It turns out that a stable symmetric solution, the Sverdrup solution with western boundary intensification, exists at small enough Reynolds numbers (see fig. 4). At $Re = 30$ a pitchfork bifurcation occurs, making the symmetric state unstable and giving rise to two stable, asymmetric states, one of which is shown in fig. 4 c The two states are each other's mirror image ($\psi_1 = \mathcal{R}(\psi_2)$). The asymmetric states become unstable themselves at $Re = 53$, where they both have a Hopf bifurcation; more Hopf bifurcations follow at still higher Reynolds numbers. These are the bifurcations which are of interest in this project. In particular, it will be investigated whether the oscillatory modes of the Hopf bifurcations can be excited by noise before actually reaching the bifurcation.

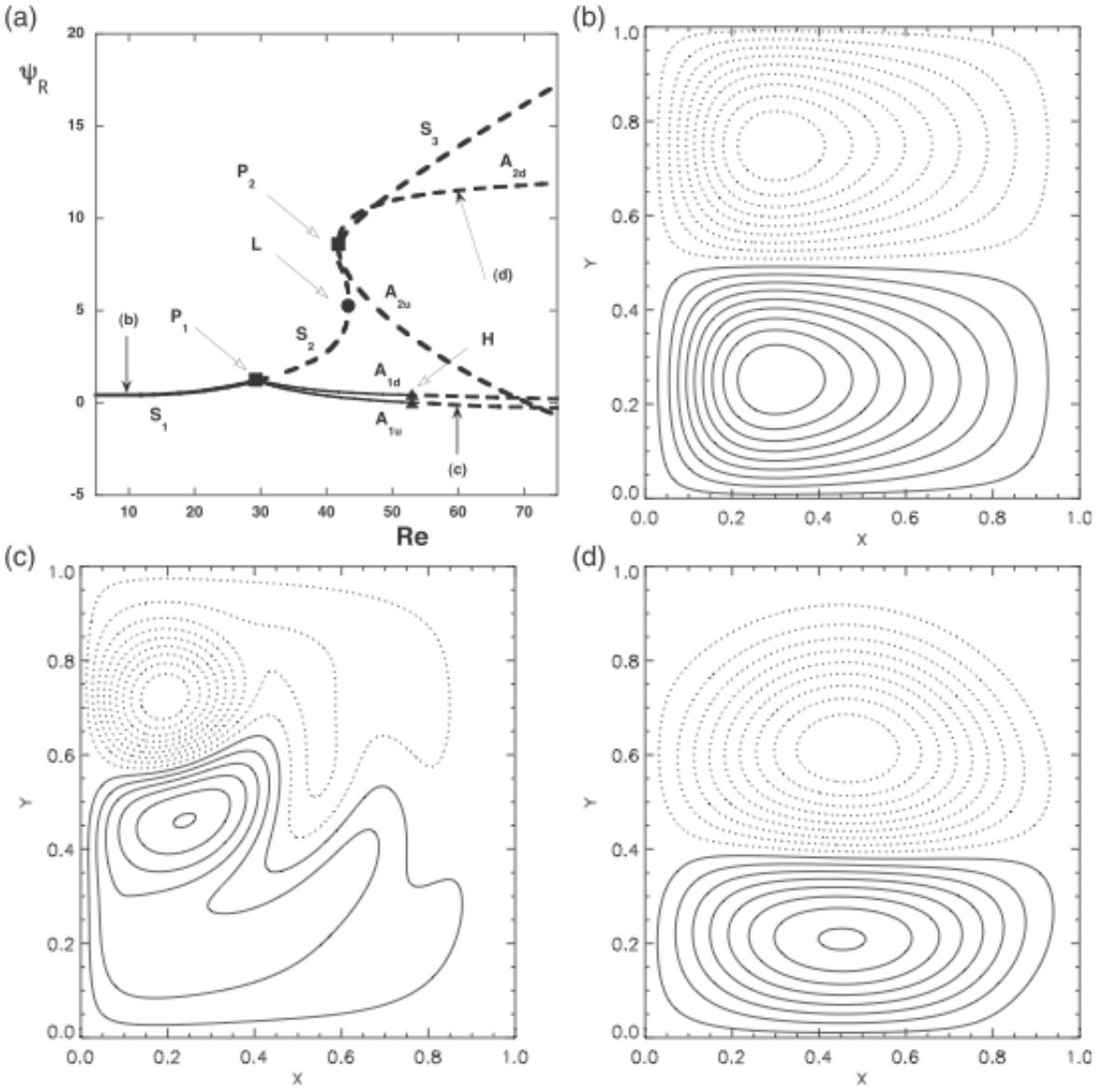

Figure 4: Solutions to eq. 29 with deterministic double gyre forcing. Panel a) shows the bifurcation diagram, where the (dimensionless) stream function ψ at location $x = L/4$, $y = L/4$ is plotted against the Reynolds number Re. Stable (unstable) branches are depicted by solid (dashed) lines. Further explanations are given in the text. - Panel b-d show the stream function at various points in the bifurcation diagram: b) at the symmetric branch S_1, c) on one of the asymmetric branches (A_{1u}) and d) on the asymmetric branch A_{2u}. The plots are taken from [Sapsis, Dijkstra 2013].

3.2 DO Equations for the Double Gyre System

The DO equations can be constructed quite easily, based on the equations 26-28 for the velocities. It is assumed that the equilibrium water depth, H, is very large ($H \gg \eta$) and bottom topography as well as bottom friction can be neglected. The Double Gyre equations then become (after a reshuffling of scaling factors; see also 1)

$$D_t u - (\bar{f} + y)v = -\partial_x p + \frac{1}{Re}\nabla^2 u + \tau^x \tag{35}$$

$$D_t v + (\bar{f} + y)u = -\partial_y p + \frac{1}{Re}\nabla^2 v + \tau^y \tag{36}$$

$$\partial_x u + \partial_y v = 0 \tag{37}$$

The wind stress contains a deterministic and a stochastic part, which will be explained in more detail below.

As described in section 2.3, we assume to solve the equations for N_{real} ocean basins simultaneously by following the mean, modes and stochastic coefficients. The only two prognostic quantities are u and v, while the pressure can be calculated from the velocities at any time: inserting eq. 35 and 36 into the time derivative of eq. 37 gives a nonlinear spatial PDE for the pressure. Hence u and v are considered "DO-variables", i.e. they are expanded as

$$\mathbf{u}(\omega) = \bar{\mathbf{u}} + Y_i(\omega)\mathbf{u_i} \tag{38}$$

where $\mathbf{u} = (u, v)$.

The expansion of the diagnostic quantity p is not of this form but follows from inserting eq. 38 into the pressure PDE.

As a metric the (depth-averaged) kinetic energy can be used:

$$< \mathbf{u_1}, \mathbf{u_2} >= \int_{\mathbf{basin}} u_1 u_2(x,y) + v_1 v_2(x,y)\ dxdy \tag{39}$$

Note that the potential energy is not part of the metric. This is handy because the metric then does not contain diagnostic quantities (pressure/sea surface height), and consistent because the kinetic energy is proportional to the water depth (the velocity is constant with depth because it is depth-averaged, and the mass of the water colums is proportional to depth), while the potential energy - rather, its deviation from the rest state - is not (it depends on surface deviations only). In the limit of very large water depth the kinetic energy dominates. More about diagnostic quantities is said in section 4.3.1.

The stochastic part of the wind forcing can in principle depend on the realisation ω: $\tau(t,x,y,\omega) = \tau_{\mathbf{d}}(t,x,y) + \sum_{\mathbf{k=1}}^{\mathbf{S_{noise}}} Z_k(t,\omega)\sigma_k(t,x,y)$ where the σ_k are spatial patterns of the noise component k, i.e. the noise is only stochastic in time.

The DO equations One can now combine the general DO-equations with the equations and definitions given above. This yields [Sapsis, Dijkstra 2013]
for the mean[3]:

$$\partial_t \bar{\mathbf{u}} = -\bar{\mathbf{u}}\cdot\nabla\bar{\mathbf{u}} - \nabla p_0 + \frac{1}{Re}\nabla^2\bar{\mathbf{u}} - f\mathbf{e}_z\times\bar{\mathbf{u}} + \tau_d - (\nabla p_{ij} + 1/2\ (\mathbf{u}_i\cdot\nabla\mathbf{u}_j + \mathbf{u}_j\nabla\mathbf{u_i}))C_{ij} + E^\omega[\sum_{\mathbf{k=1}}^{\mathbf{S_{noise}}} Z_k(t,\omega)\sigma_k(t,x,y)] \tag{40}$$

$$\nabla\cdot\bar{\mathbf{u}} = 0 \tag{41}$$

for the modes:

$$\partial_t \mathbf{u}_i = \mathbf{Q}_{\mathbf{u},i} - < \mathbf{Q}_{\mathbf{u},i}, \mathbf{u_j} > \mathbf{u}_j \tag{42}$$

$$\nabla\cdot\mathbf{u_i} = 0 \tag{43}$$

with the definitions

$$\begin{aligned}\mathbf{Q}_{\mathbf{u},i} &= \nabla p_i + \frac{1}{Re}\nabla^2\mathbf{u}_i - \mathbf{u}_i\cdot\nabla\bar{\mathbf{u}} - \bar{\mathbf{u}}\cdot\nabla\mathbf{u}_i - f\mathbf{e}_z\times\mathbf{u}_i + (\nabla p_{mn} - \frac{1}{2}(\mathbf{u}_m\cdot\nabla\mathbf{u}_n + \mathbf{u}_n\cdot\nabla\mathbf{u}_m))C^{-1}_{ij}C_{jmn} + \\ &\quad E^\omega[Y_j(\omega)Z_r(\omega)](-\nabla b_r + \sigma_r)C^{-1}_{ij}\end{aligned} \tag{44}$$

[3]the last term in eq. 40 drops out if the forcing is chosen to be zero-mean.

and constraints for the pressure:

$$\nabla^2 p_0 = \nabla \cdot (-\bar{\mathbf{u}} \cdot \nabla \bar{\mathbf{u}} - f\mathbf{e}_z \times \bar{\mathbf{u}} + \tau_d) \tag{45}$$

$$\nabla^2 p_i = \nabla \cdot (-\mathbf{u}_i \cdot \nabla \bar{\mathbf{u}} - \bar{\mathbf{u}} \nabla \cdot \mathbf{u}_i - f\mathbf{e}_z \times \mathbf{u}_i) \tag{46}$$

$$\nabla^2 p_{ij} = \frac{1}{2} \nabla \cdot (\mathbf{u}_i \cdot \nabla \mathbf{u}_j + \mathbf{u}_j \nabla \cdot \mathbf{u}_i) \tag{47}$$

$$\nabla^2 b_r = \nabla \cdot \sigma_r \tag{48}$$

also recall the definition for the correlation operator:

$$C_{ijk\ldots} = E^{\omega}[Y_i(\omega) Y_j(\omega) Y_k(\omega) \ldots] \tag{49}$$

For the evolution of the stochastic coefficients, the following equation holds:

$$dY_i/dt = A_{ij} Y_j + B_{ijk} Y_j Y_k + D_i \tag{50}$$

with

$$A_{ij} = < \frac{1}{Re} \nabla^2 \mathbf{u}_j - \mathbf{u}_j \cdot \nabla \mathbf{u}_j \ , \ \mathbf{u}_i > \tag{51}$$

$$B_{ijk} = -\frac{1}{2} < \mathbf{u}_j \cdot \nabla \mathbf{u}_k + \mathbf{u}_k \cdot \nabla \mathbf{u}_j \ , \ \mathbf{u}_i > \tag{52}$$

$$D_i = B_{ijk} C_{jk} + < \sigma_r \ , \ \mathbf{u}_i > Z_r \tag{53}$$

3.3 Simulation settings

In this project, the basin length is $1000km$ and a grid of 96×96 points; this is a rather coarse resolution but in [Sapsis, Dijkstra 2013] it is demonstrated that the difference betweenruns with 64, 96 and 128 grid points is only a few procent, so 96×96 gid points seems a good compromise between computation time and resolution. The integration time is $T = 11$ (dimensionless time), which corresponds to approximately 22 years; this time is chosen because it is well after the spinup. As time step size, 10^{-4} is used, except for very high Reynolds numbers ($Re = 54$), for which this proved to coarse. The number of realisations is 1000 and the number of modes is fixed to be 6.

The deterministic part of the wind stress is given by

$$\tau^x = -\tau^0 \cos(2\pi y) \ , \ \tau^y = 0$$

where $\tau_0 = 1000/2\pi$.

The stochastic part, which in general has the form $\sum_{\mathbf{k=1}}^{\mathbf{S_{noise}}} Z_k(t,\omega)\sigma_k(t,x,y)$ consists of one noise component (spatial pattern), i.e. $S_{noise} = 1$, and the stochastic amplitude of it does not depend on the realisation here. The noise forcing is given by

$$\tau^x_{stoch} = \tau^0 A \eta(t) f(x,y) \ , \ \tau^y_{stoch} = 0 \tag{54}$$

with the spatial pattern

$$f(x,y) = \alpha/\sqrt{\pi} \ [\lambda \, \mathrm{Erf}(1/2\lambda)]^{-1} \exp[\frac{(x/L - 1/2)^2 + (y/L - 1/2)^2}{2\lambda^2}] \tag{55}$$

where $\alpha = 1/f(0,0)$ is a normalisation constant and λ determines the spatial extension of the noise; here it is taken to be $\lambda = 1/3$. A is a scaling factor for the noise amplitude. In this project $A = 0.05$, even though this is rather low compared to the determinitic part of the wind stress, because otherwise the code crashes - at least for this rather low time resolution.

The temporal pattern of the noise is given by η, where η is either white noise $W(t)$ (Gaussian random number at each time step) or red noise, which is given by [Sapsis, Dijkstra 2013]:

$$d\eta(t) = -\frac{1}{\tau}\eta(t)\,dt + \sqrt{2/\tau}\,dW(t) \tag{56}$$

Note that in principle, η and W depend on the realisation ω.

Before actually taking data, a few preliminary runs with no noise were performed in order to to verify the location of the first Hopf bifurcation - this can vary a little, depending on resolution. It as found that the Hopf bifurcation indeed lies near $Re = 53$. This was concluded from the appearence of non-decaying oscillatory modes.
Since the main focus lies on the behaviour of the double gyre system before the first Hopf bifurcation, calculations were performed for the Reynolds numbers $Re = 42, 46, 50, 52$, for zero noise, white noise and red noise. The decorrelation time of the red noise is $\tau = 0.5$ (roughly one year), $\tau = 1$ and $\tau = 2$. Finally, two runs were performed for $Re = 54$ (just after the first Hopf) for red ($\tau = 0.5$) and white noise.

As the modes and coefficients usually do not vary at the time scale of the time step dt, data is written out every 100 timesteps, in dimensional time units this means 100 times in 2 years or about once per week.
The parameter space up to $Re = 40$ has already been investiated [Sapsis, Dijkstra 2013].

3.4 Results Double Gyre

In this section I only show a selection of the plots made of the mean and modes; the complete plots are given in the appendix.

3.4.1 Bimodality

In fig. 5, the mean, first mode and histogram of the coefficients for the first mode are shown. The settings for this figure are $Re = 46$, white noise, and the time is $t = 9.5$ (about 19 years), but very similar results are found for all runs except $Re = 54$, white noise.

The mean state is symmetric against mirror reflection around $y = 1/2$, while the first mode is antisymmetric and has a bimodal probability distibution. This behaviour is due to the pitchfork bifurcation at $Re \approx 30$. From fig. 6 one can see that after an initial spin-up the variances

$$Var_i = \sum_{\omega=1}^{N_{Real}} (Y_i(\omega))^2$$

of all but the first mode decrease very rapidly (exponentially), while the variance of the first mode equilibrates to values near the energy of the mean[4]. This means that the realisations equilibrate towards one of the two stable pitchfork branches. The pitchfork branches of this Double Gyre model correspond to the two modes of the Kuroshio current. However, the realisations do usually not 'switch' between pitchfork branches after the spinup time in my data (something which does happen in the real Kuroshio current), but they might do so for larger noise amplitudes. For example, for $Re = 54$, red noise ($\tau = 0.5$) and $Re = 42$, $\tau = 2$ the decay starts much later then for smaller Re before the Hopf.

Apart from decaying, the time series of the variance of the transient modes also shows oscillatory behaviour, at periods of about a year (mode 2,4) and a few months (mode 5). It is interesting that one sees oscillations in the variance which is a quantity formed by all realisations together: The realisations have to behave somehow collectively.

For $Re = 54$ and white noise, mean and first mode are very different from the other cases (fig. 7), because the model landed in the 'inertial' regime (panel d of fig. 4).

Bimodality has also be found for lower Reynolds numbers in [Sapsis, Dijkstra 2013]

3.4.2 Variance

In order to see how noise forcing affects the variability, the variance of different quantities (zonal and meridional velocities and kinetic energy) was calculated at several locations, $\mathbf{x_1} = (1/6, 1/2), \mathbf{x_2} = (1/4, 1/4), \mathbf{x_3} = (2/3, 1/2), \mathbf{x_4} = (1/4, 3/4)$ and times $t = 8$, 10.99 (i.e. after the spinup). The dominant, but not very interesting contribution to the variance comes from the pitchfork mode; in order to filter this out, the realisations were sorted according to their pitchfork branch and then the variance was calculated per branch. The results for the first two locations are shown in fig. 8-9; the other two yield very similar outcomes; one can also see from the figure that the results are very robust against the choice of quantity or location.

[4]since the energy is used as metric and the modes are normalised to $< \varphi, \varphi >= 1$, the variance of a mode equals the energy associated with the mode, hence it makes sense to compare the energy of the mean to the vatiance of the modes.

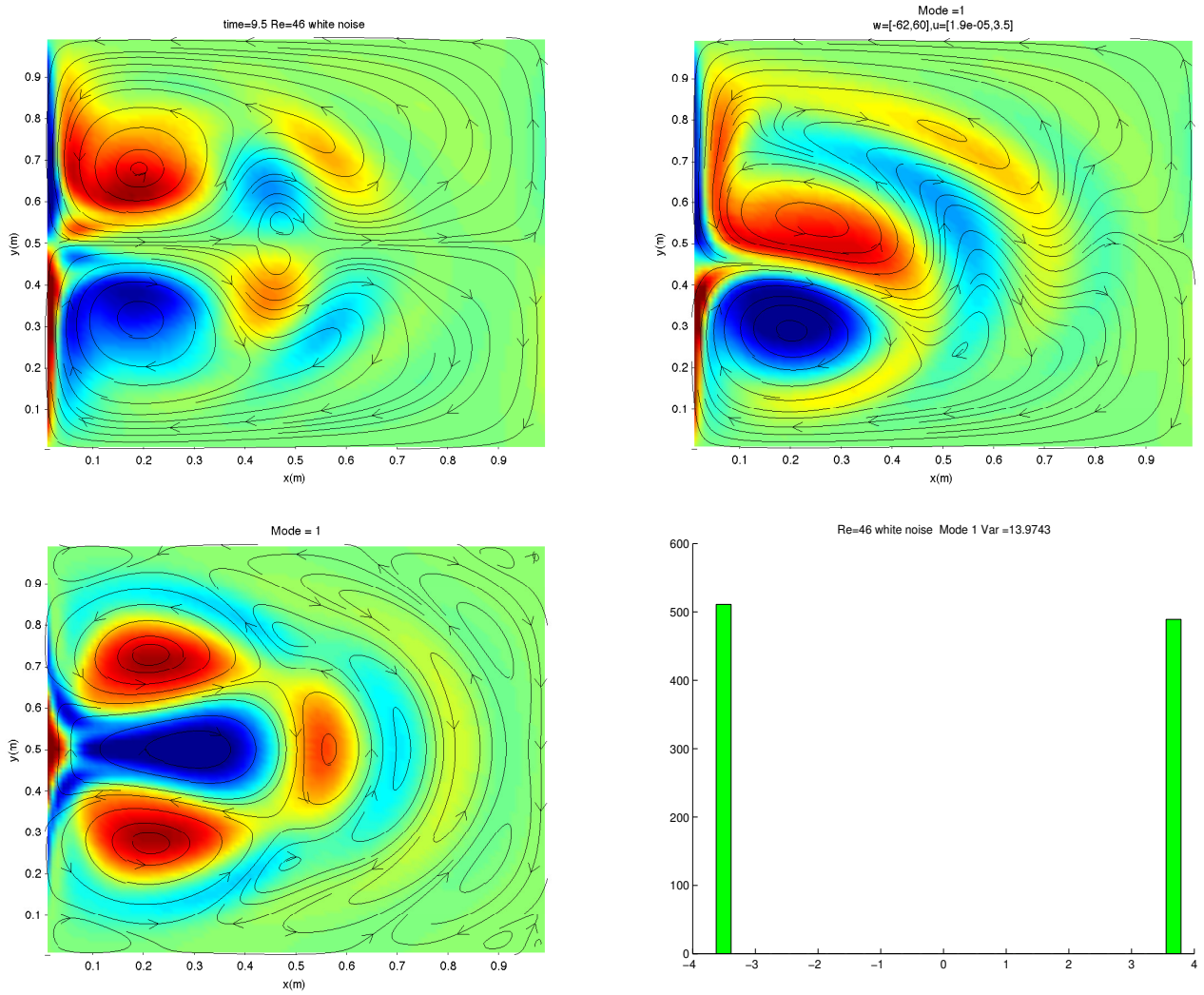

Figure 5: Results for $Re = 46$, white noise. The top left panel shows the mean state, the bottom left one the first mode. The bottom left panel shows the histogramm over the realisatons for the stochastic coefficients associated to the first mode, and the top right panel shows one realisation. Since all but the first mode have a very small variance, the realisation is mainly dominated by the mean and the first mode.
Colours depict vorticity: blue corresponds to negative and red to positive vorticity. The contours are streamlines.

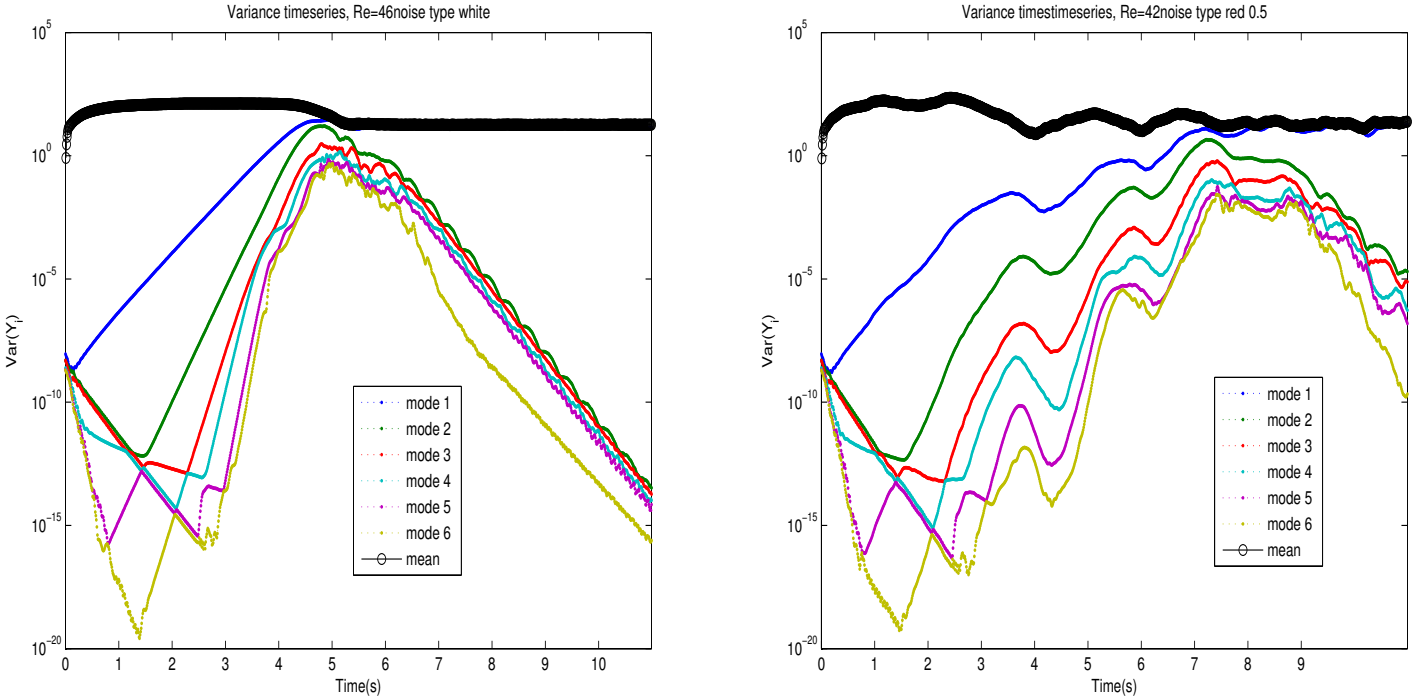

Figure 6: Timeseries of the energy of the mean state (black) and the variance associated to the modes for $Re = 46$, white noise and $Re = 42$, red noise ($\tau = 2$).

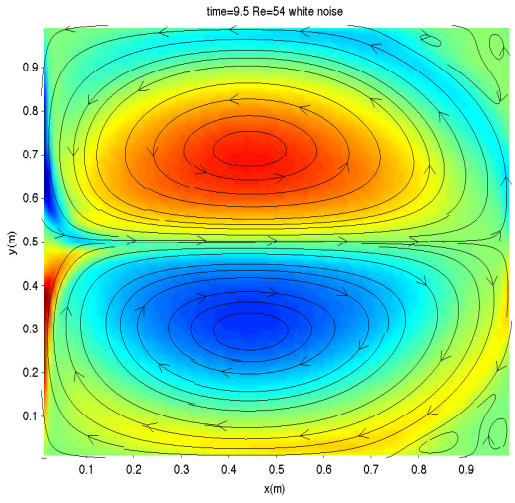

Figure 7: mean state for $Re = 54$, white noise. Colors depict vorticity: blue corresponds to negative and red to positive vorticity. The contours are streamlines.

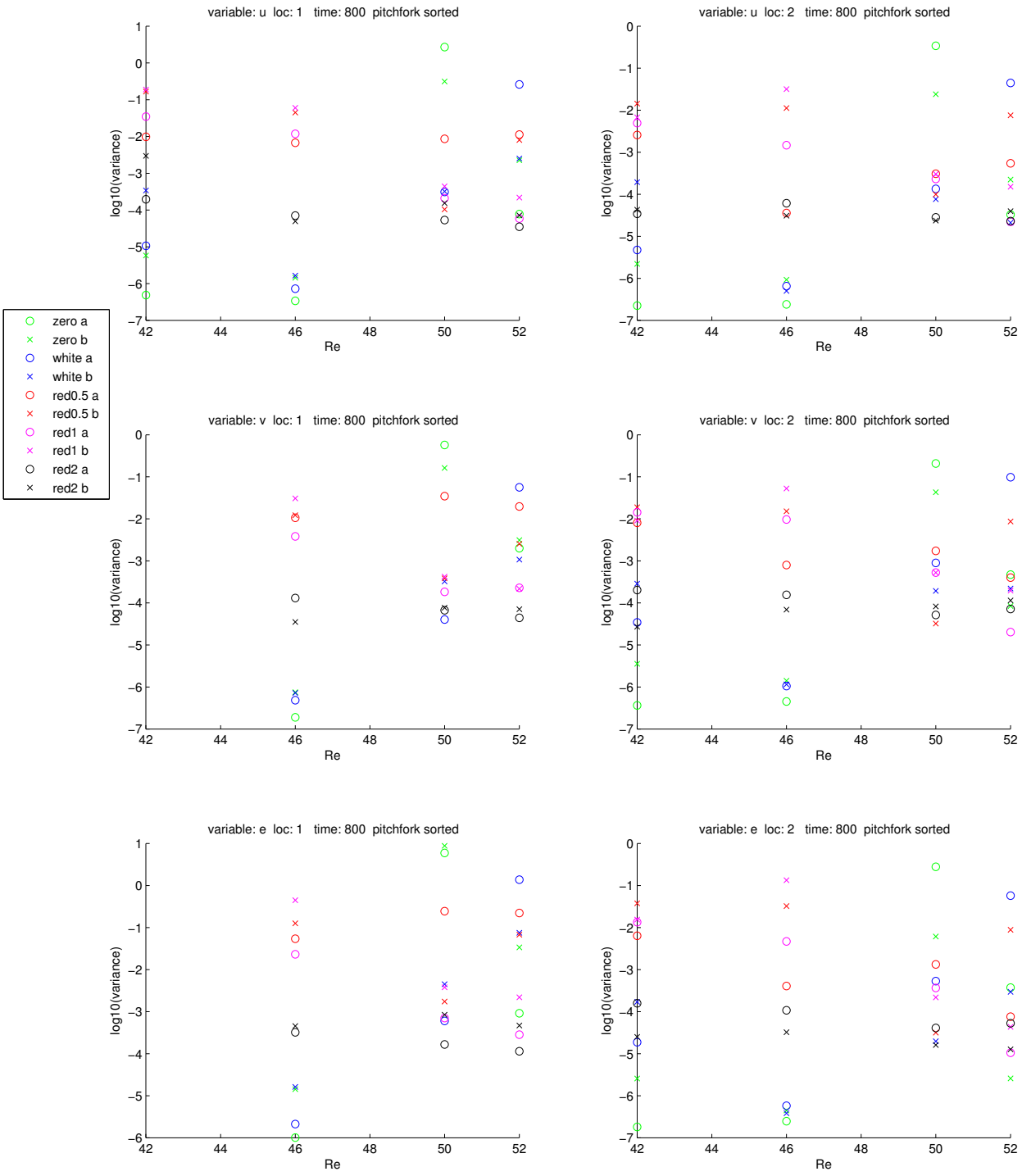

Figure 8: The total variance of zonal/meridional velocity and kinetic energy at the locations $(x_1 = 1/6, y_1 = 1/2)$ and $(x_2 = 1/4, y_2 = 1/4)$, plotted against Reynolds number for all noise types (green symbols: no noise; blue: white noise; red, magenta, black: red noise with $\tau = 0.5, 1, 2$), and crosses/circles are used for the two pitchfork branches), at time $t = 8$.

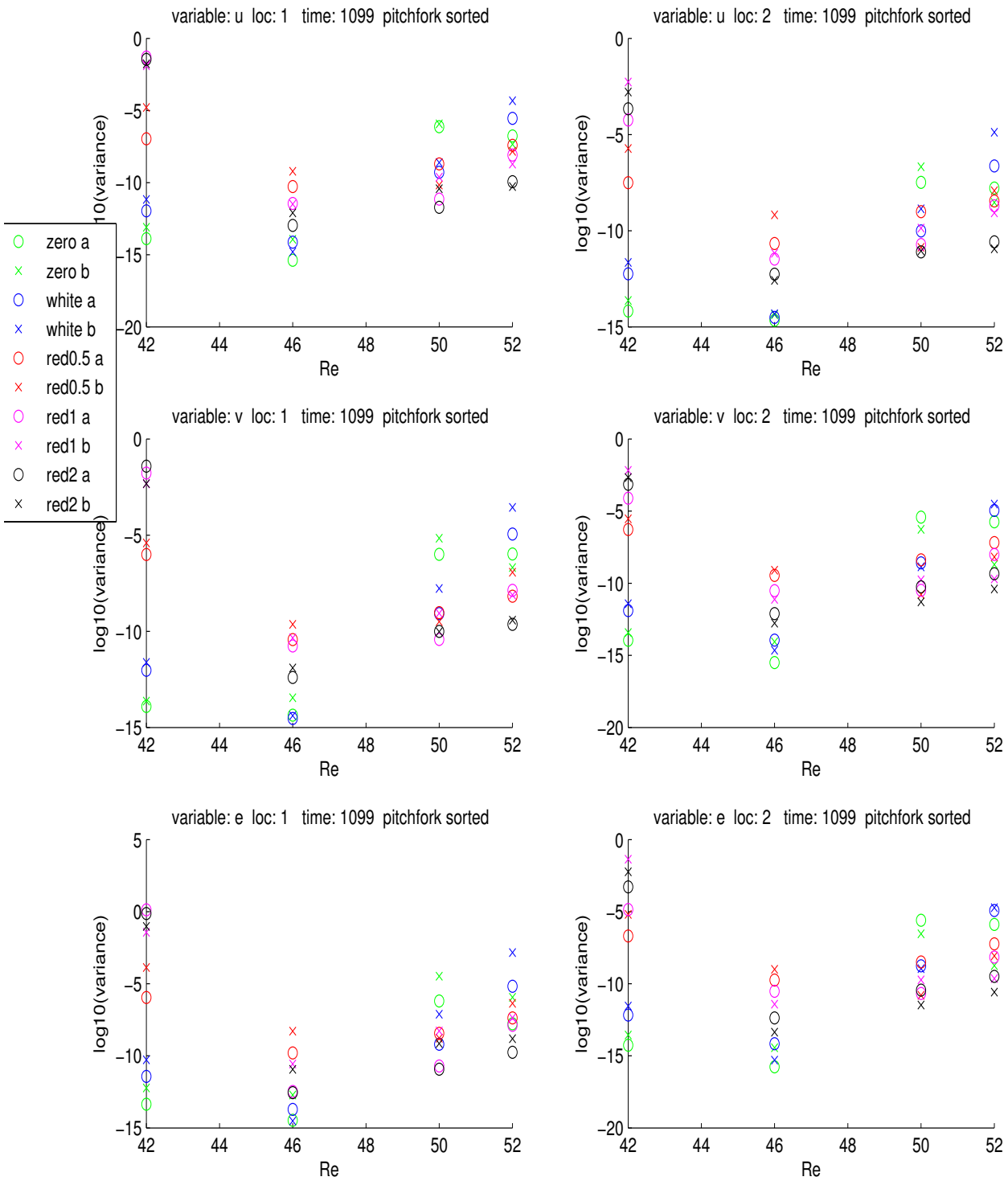

Figure 9: The total variance of zonal/meridional velocity and kinetic energy at the locations $(x_1 = 1/6, y_1 = 1/2)$ and $(x_2 = 1/4, y_2 = 1/4)$, plotted against Reynolds number for all noise types (green symbols: no noise; blue: white noise; red, magenta, black: red noise with $\tau = 0.5, 1, 2$), and crosses/circles are used for the two pitchfork branches), at time $t = 10.99$.

At $t = 8$ the variance is much higher than at $t = 10.99$, which is no surprise because the moderwise variance decays for all but the first mode There is an exception, though, namely $R = 42$, $\tau = 2$. For $t = 8$ the range of variances is smaller than for $t = 10.99$ - less time has elapsed since the end of the spin-up, where the variance is rather similar for all runs - and the difference between Reynolds numbers less large, with high Re reaching slightly larger variances. There is no clear result about how the variance depends on the noise and Re. At $t = 10.99$ the variances are comparable for $Re = 52$, $Re = 50$, and $Re = 42$ with red noise, while $Re = 46$ produces far smaller variances. Higher variance at high Re is to be expected, because one is closer to the Hopf bifurcation that is supposed to be excited. The fact that $Re = 42$ gives larger variances than $Re = 46$ for all noise types, and even the highest variances of all runs ($\tau \geq 1$) is harder to explain, it might for example be that the 'potential well' causing the pitchfork is shallower at $Re = 42$ - the excitation might then not be related to the Hopf at $Re = 53$.

The dependence of the variance on the noise type is very strong, but not very systematic. At $Re = 42$, red noise produces the largest variances, while at $Re = 52$ the variance is largest for white noise and decreases with decorrelation time for red noise. This might suggest that at low Re variance is associated with low-frequency fluctuations, while at high Re fluctuations have higher frequencies. At $Re = 46$ red noise with $\tau = 0.5$ generates the highest variance, while both white noise and red noise with longer decorrelation time are less efficient. A very puzzling result is that for $Re = 50$ the variance is highest for zero noise. This certainly requiress closer investigation.

3.4.3 Fourier spectra of the energy

Hopf bifurcations cause oscillatory behaviour, hence it is interesting to have a look at Fourier spectra of the kinetic energy (fig. 10-11), both with and without the modes included. In the latter case, the absolute values of the Fourier coefficients of the mean state energy at the four locations $\mathbf{x_1} = (1/6, 1/2), \mathbf{x_2} = (1/4, 1/4), \mathbf{x_3} = (2/3, 1/2), \mathbf{x_4} = (1/4, 3/4)$ are calculated and the mean is taken over the locations. In the first case, the same is done for all realisations seperately and then the mean is also taken over the realisations. The time range is $8.5 < t < 10.5$ (dimensionless time), i.e.after the spinup, except for $Re = 54$ where $9.5 \leq t < 11$ is chosen in order to avoid the spin-up during which the pitchfork is not yet developed (so the results are not comparable to the other Re)

The energy of the spectrum is higher for the realisationwise Fourier transform than for the mean. This suggests that the mean is more 'static' while the modes contribute strongly to the fluctuation in time. The difference between realisationwise and mean spectra is especially large for $Re = 54$ where the variance has not yet decayed so much.

The fact that the mean state shows time variability at all might be due to interaction with the modes, or to direct forcing, because the noise is not zero-mean (as it is the same for all realisations).
For all Reynolds numbers there is a rather strong peak near frequency $0.1 months^{-1}$ (10 months period). It exists for almost all types of noise, but the values are several orders of magnitude higher for red noise of short decorrelation time than for white or zero noise - even for high Reynolds numbers, where the variance is highest for zero ($Re = 50$) or white ($Re = 52$) noise. The peak is also strong in the Fourier spectrum of the mean state. This peak will turn out to belong to the second Hopf bifurcation. Due to its long period it is excited more easily by red noise.

Another noticeable peak lies at $0.5 months^{-1}$(period 2 months). It appears at all Reynolds numbers but is less pronounced at $Re = 42$ and most significant for $Re = 50$. For low Reynolds numbers it is a actually a double peak with a marked dip; for $Re = 52$ the dip becomes weaker. At low Reynolds numbers it is only seen in the presence of noise, while at $Re = 50$ and $Re = 52$ it is especially strong for zero noise. This peak is linked to the first Hopf bifurcation. Interestingly the two-monthly peak at $Re = 54$ (beyond the Hopf bifurcation!) is not very pronounced.

It is necessary to perform a significance test here in order to be sure that these peaks are not - possibly - just noise. Due to lack of time this has been omitted.

3.4.4 Transient modes

Comparing the Fourier spectra of the Y to the plots of the modes, one can reconstruct which modes belong to which frequencies.

Apart from the pitchfork mode there are two interesting modes which have a transient behaviour. They are linked to the first two Hopf bifurcations on the pitchfork branches. Only a few nice examples of these modes are shown here; when looking at all modes, one will also find many deformed or hybrid versions.

The Gyre mode The Gyre mode [Simmonet, Dijkstra 2002]can be found for many runs, in fig. 12 the example $Re = 42$, red noise is chosen. For this run, mode 2 and 3 are approximately each other's mirror image (one has to multiply one of the modes by -1, which does not alter the realisations - the physical quantities - if one simultaneously switches the sign of the stochastic coefficients Y_i). When considering the scatter plots of the $Y_i (i \in \{2, 3\})$ against Y_1, one sees that mode 2 (3) only has a strong variance at the pitchfork branch with positive (negative) coefficients Y_1.

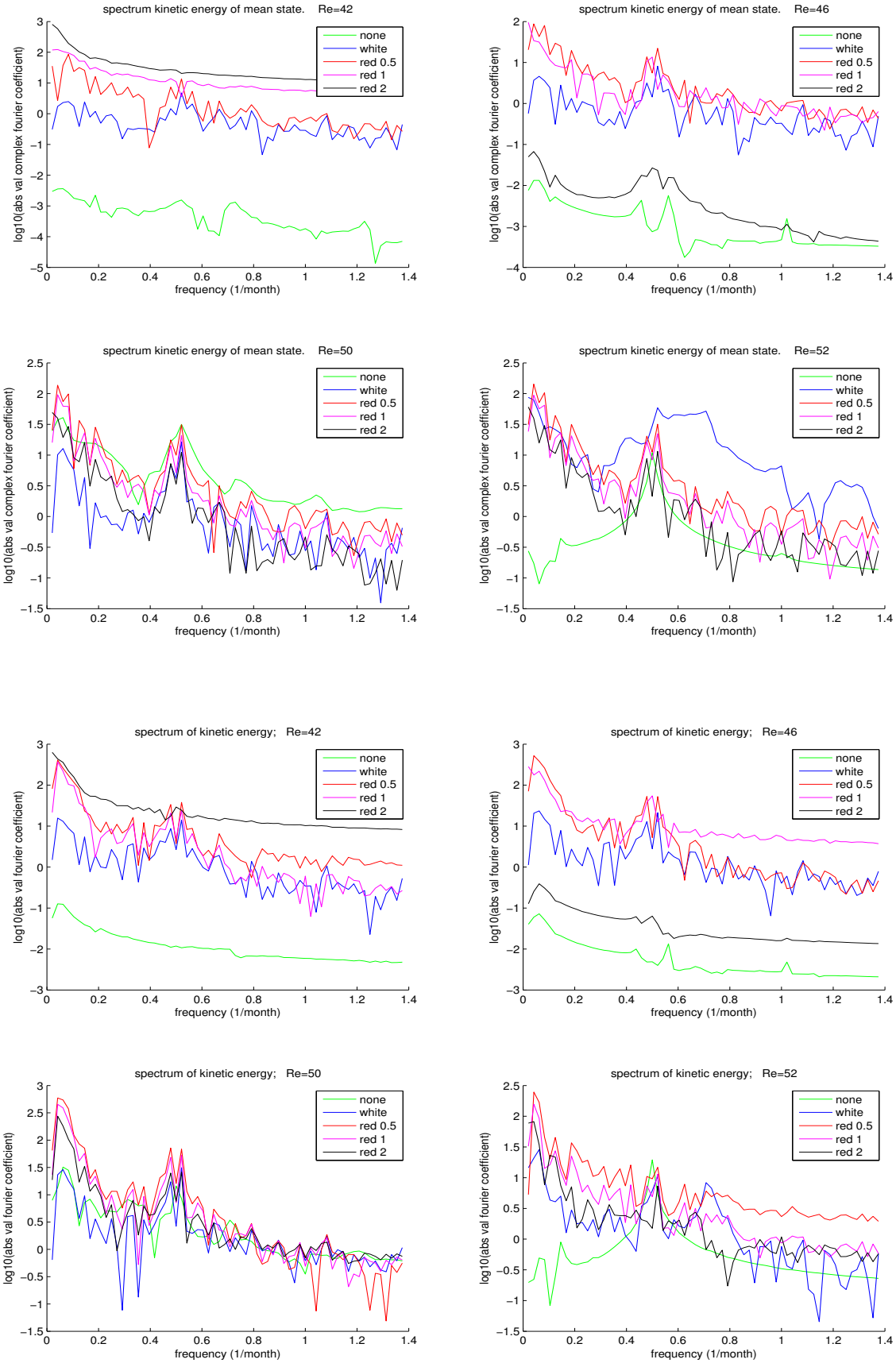

Figure 10: Fourier spectra for the energy. In the upper four plots, the Fourier spectrum is calculated realisationwise, and the mean of the absolute values is taken; in the lower plots, the energy of only the mean state is taken. In both groups, the top left plot is for $Re = 42$, top right: $Re = 46$, bottom left/right: $Re = 50/52$.

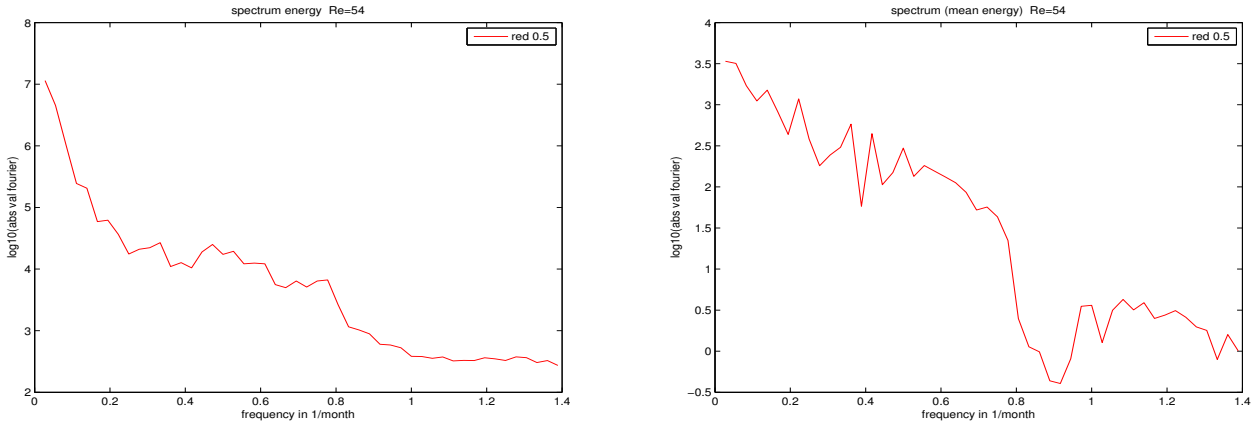

Figure 11: As figure 9 but for $Re = 54$, red noise with $\tau = 0.5$. The realisationwise spectrum is in the left panel, the mean state in the right one.

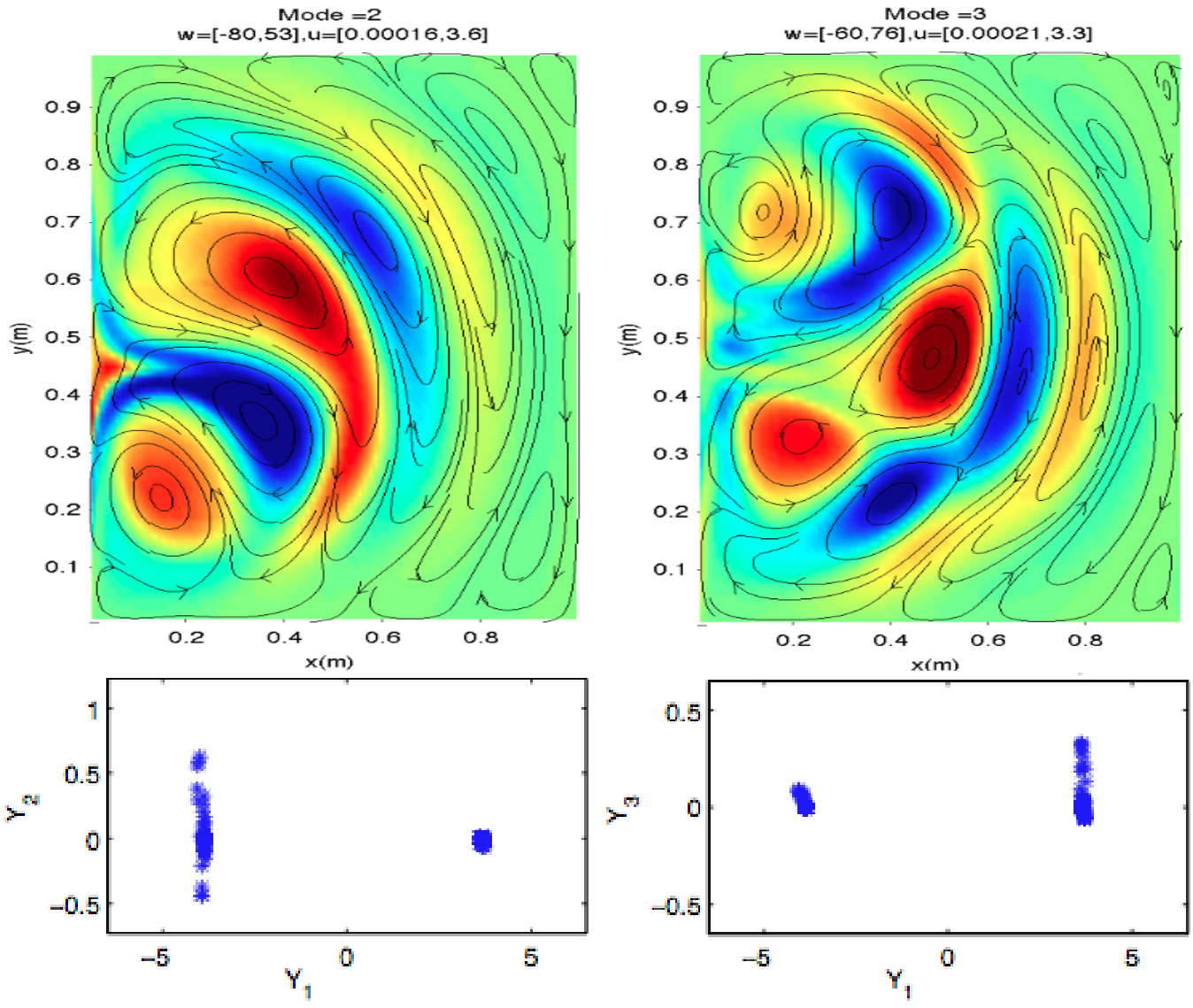

Figure 12: The Gyre mode. The upper plots show the mode 2 and 3 for $Re = 42$, red noise. The lower panels are scatter plots of the coefficients Y_2 (Y_3) against Y_1.

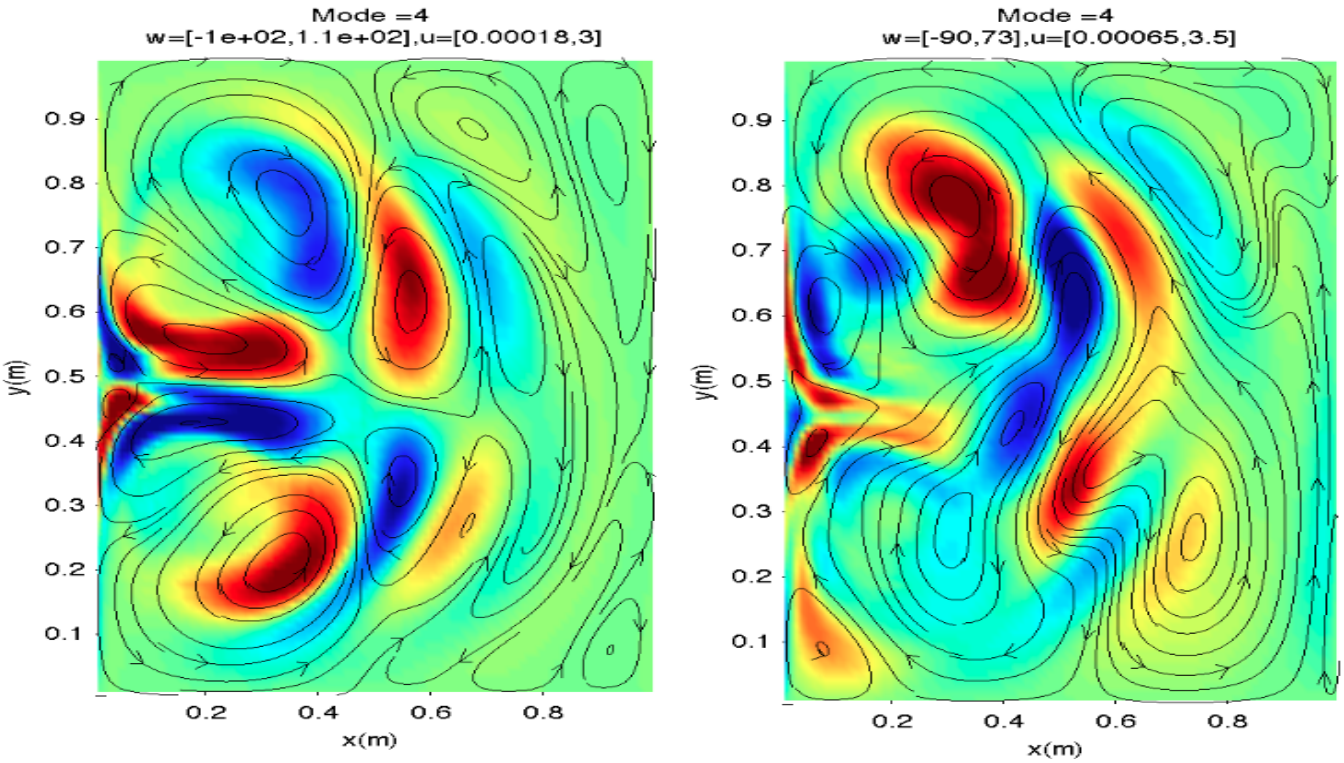

Figure 13: Rossby basin mode. The plots are for $Re = 42$,red noise (left) and $Re = 50$, white noise (right).

So apparently there is one Gyre mode for each pitchfork branch. This result is in agreement to earlier research (see [Dijkstra 2005]). However, the 'sorting' according to the pitchfork branch is not always as clear as for this run (see, for example, $Re = 42$, white noise)

The Gyre modes are associated to the second Hopf bifurcation (at $Re \approx 80$). Physically, they strengthen and weaken the jet periodically. The actual period is about 3 years, but in these simulations the period is reduced to about one year (dimensionless time: 0.5), as one can see when looking at spectra of the Y belonging to that mode. The reduction in period is due to the smaller basin length ($1000km$).

Interestingly this mode can be excited even very far from the corresponding Hopf bifurcation.

The Rossby basin mode The Rossby basin modes are similar to free Rossby waves, but in a bounded domain, i.e. they have to fullfill boundary conditions. In a square basin, they obey

$$\psi(x, y, t) = A \sin(n\pi x) \sin(m\pi y) \exp[-i(\sigma_{nm} t + \frac{\beta x}{2\sigma_{nm}})]$$

with

$$\sigma_{nm} = -2\beta/\sqrt{(n\pi)^2 + (m\pi)^2}$$

(Constant density is assumed, hence only the barotropic case is considered). With $\beta = \beta_0 L^2/U \approx \frac{10^{-11}(ms)^{-1} \times (10^6 m)^2/}{1m/s} = 10$ and $m = n = 2$ one obtains

The 7-monthly variability in fig. 1 is due to Rossby basin modes. As for the Gyre modes the period in my simulations is reduced by a factor of about 3 with respect to observational data; the peak at 2 months period in the Fourier spectra comes from the Rossby basin modes.

The Rossby basin mode belongs to the Hopf bifurcation at $Re = 53$. In order to find out whether it shows coherence resonance behaviour, one can compare the variance of the highest mode resembling a Rossby basin mode for various Re and the noise type. Unfortunately there are some doubtfull cases where it is hard to decide whether the mode is a Rossby basin mode or not. Also the spin-up takes more time in certain runs, for example, $Re = 42$ and long noise correlation times. Thus the data is a bit insufficient but seems to suggest that Rossby basin modes can be excited at lower Reynolds numbers by red noise with $\tau \lesssim 1$, while for Reynolds numbers closer to the Hopf bifurcation they even occur without noise (having been excited during the spinup). This hints at coherence resonance behaviour.

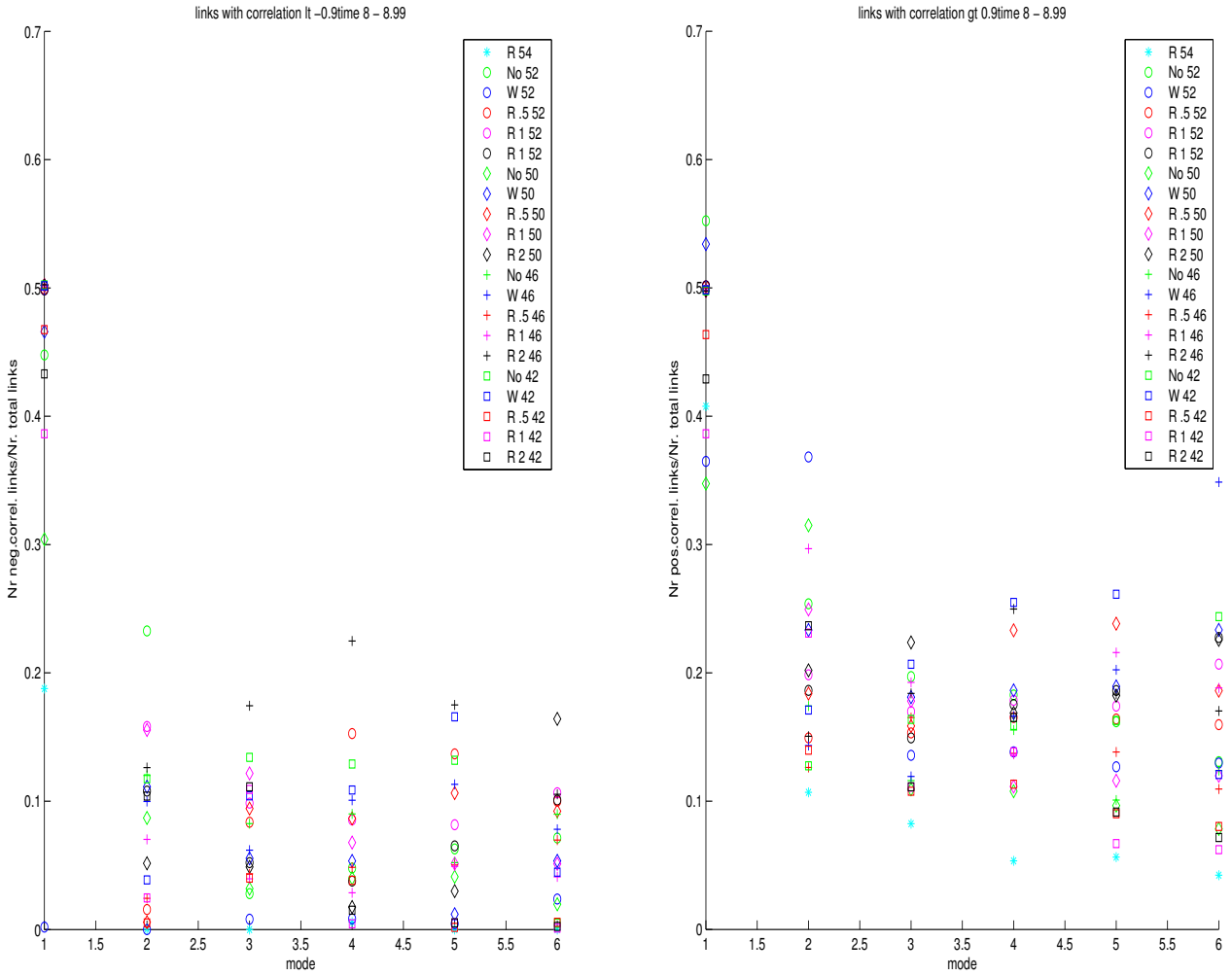

Figure 14: Synchronisation of the stochastic coefficients in the time range $8 \leq t \leq 8.99$; left: negative, right: positive correlation. In all cases, $N_{C(A)}/N_P$ (number of (anti)correlated pairs over total number of pairs) is plotted against the mode.

For $Re = 54$, i.e. past the Hopf bifurcation, all but the first (pitchfork) mode look like Rossby basin modes - in fact, they bear a rather close resemblance to the various phases of the Rossby basin mode described in [Dijkstra,Katsman 1997]. Not surprisingly, modes 2-5 have a much higher variance than for lower Re. However, in fig. 6 one sees that also for $Re = 54$, $\tau = 0.5$ their variances start to decay, but later than for most other runs. It is not clear from the data whether the decay continues or an equilibrium is reached. One would expect the variance of the Rossby basin modes to equilibrate to a non-zero value past the Hopf bifurcation.

3.4.5 Synchronisation

While looking at time series of different realisations the Y_i one can see that they often look quite 'synchronised'. In order to quantify this observation, the correlation in time (for $8 \leq t \leq 8.99$ and for $10 \leq t \leq 10.99$) of all possible pairs formed of the first 200 realisations (with $N_{pair} = 200 \times 199/2$) was calculated. When two realisations have a correlation higher then $L \equiv 0.9$ (lower then $-L$) they are considered (anti)'linked'. The number of (anti)correlated pairs is denoted by N_A, N_C . In fig. 14, $\frac{N_A}{N_P}$ and $\frac{N_C}{N_P}$ are plotted for each mode, Reynolds number, noise type and time

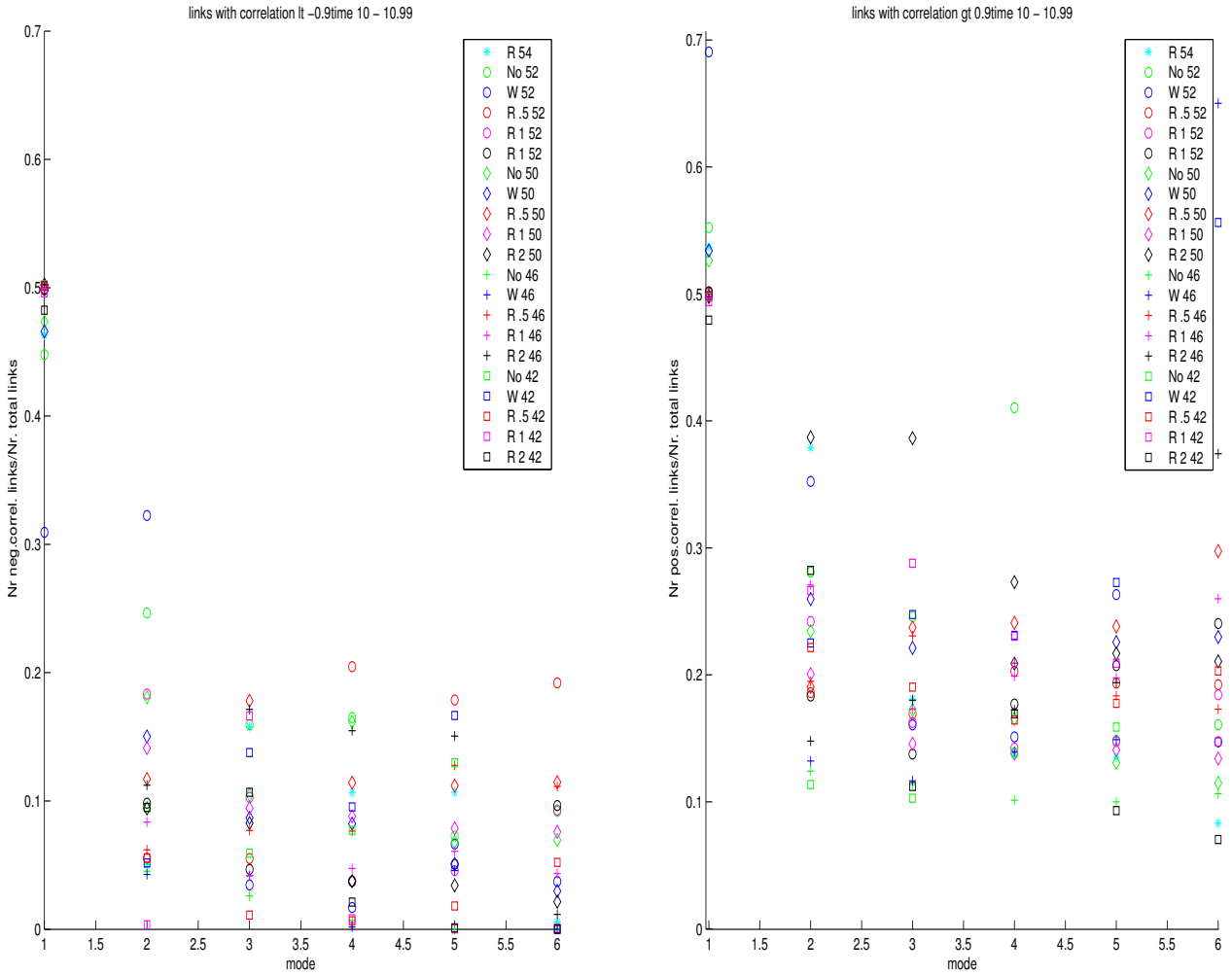

Figure 15: Synchronisation of the stochastic coefficients in the time range $10 \leq t \leq 10.99$; left: negative, right: positive correlation. In all cases, $N_{C(A)}/N_P$ (number of (anti)correlated pairs over total number of pairs) is plotted against the mode.

range. [5]

It turns out that mode 1 has very high (anti)links, namely both around 1/2: the realisations are divided into two groups which evolve in an opposite way. (It migth be interesting to check whether these groups are connected to the pitchfork branches.) For the other modes, the number of (anti) linked pairs is about (0-20%) 10-30% of the possible pairs. There is no strong trend in time. Globally, white noise produces the most positive links, followed by red noise with $\tau = 0.5$. Noise with high correlation time and zero noise produce less (positive) links in general, but there are exceptions (mode 4, zero noise, $10 \leq t < 11$). For $Re = 54$ there are very few positive links for $8 \leq t < 9$ but significantly more at $10 \leq t < 11$. Compared to the other runs, the decay of the variances starts much later in this run; maybe synchronisation is an effect which only sets in after the spin-up.

I suspect that synchronisation is due to the fact that the 'stochastic' forcing does not depend on the realisations. So the realisations only differ in their initial conditions but get the same 'input' during the time evolution. During the decay, when the variance becomes small and hence there is little interaction between the modes, the synchronisation effect is probably especially large.

I also suspect that synchronisation might lead to a decrease in the variance. After all, if many realisations fluctuate in the same way, this becomes a fluctuation of the mean. One could check this by calculating the energy transfer between the modes and the mean. It would also be interesting to do a run with realisation-dependent forcing.

4 El Niño/Southern Oscillation

4.1 ENSO and the Zebiak-Cane model

The Zebiak-Cane model is a rather simple model which nevertheless captures the main features of ENSO. It contains a reduced-gravity model oceanic part, with the thermocline as boundary between the less dense active layer and the dense lower layer; within this upper layer, it has a surface layer with the sea surface temperature (SST) and Ekman dynamics; and an atmosphere which, for simplicity, is described by a shallow water model.

As the model area does not extend too far off the equator (about 30^o), a β-plane approximation is made, i.e. one uses Cartesian coordinates and the Coriolis parameter $f = 0 + \beta y$.

In this thesis, the model is run in an anomaly mode, i.e. one calculates the deviations from a prescribed, season-dependent background state.

In the following I will briefly explain the equations of the Zebiak-Cane model. Note that here all quantities are dimensional.

4.1.1 System Equations

The ocean is modelled as an 1.5layer or reduced gravity model where the active upper layer (average depth H) obeys shallow water equations as a whole but is subdivided into a main part (depth H_2) and a well-mixed surface layer (depth H_1). This is done to incorporate Ekman dynamics. Also it will be the mixed layer whose temperature is coupled to the atmosphere.

We define the following oceanic velocities:

$$\mathbf{u_1} = \frac{1}{H_1}\int_{-H_1}^{0} \mathbf{u}dz \ , \ \ \mathbf{u_2} = \frac{1}{H_2}\int_{-H_2}^{-H_1} \mathbf{u}dz \ , \ \ \mathbf{u}_m = \frac{1}{H}\int_{-H}^{0} \mathbf{u}dz \ , \ \ H = H_1 + H_2$$

The "extra Ekman effect" in the mixed layer is described by $\mathbf{u_s} = \mathbf{u_1} - \mathbf{u_m}$. From now on, $\mathbf{u}_m$ will be denoted by $\mathbf{u}$.

Reduced gravity model The momentum balance equations (first, in the zonal direction, than meridional) read:

$$\partial_t u + a_m u - \beta_0 y v + g' \partial_x h = \frac{\tau_x}{\rho H} \tag{57}$$

$$\eta \partial_t v + a_m v + \beta_0 y u + g' \partial_y h = \frac{\tau_y}{\rho H} \tag{58}$$

[5] When dealing with timeseries of Y one has o take into account that the code always numbers the modes according to their contribution to the variance, i.e. the dominant mode is called mode 1 etc. When mode i becomes more dominant than mode $i-1$, they will exchange their indices. One therefore has to re-order the modes, with a procedure based on the orthonormality of the modes at any time and assuming that the modes do not change strongly in time, in order to obtain proper time series of the Y.

Here u and v denote the zonal and meridional velocity component, respectively. The terms describe, from left to right: the time derivative, (frictional) damping, the Coriolis effect on the β-plane, pressure gradient force due to deviations of the thermocline depth, and the wind stress. Note that the non-linear advection terms have been ignored.

Since the zonal scale of ENSO is so much larger than the meridional scale, one can leave out the time derivative term in the meredional momentum balance ($\eta = 0$). This will remove short waves. (See [Dijkstra 2005] chapter 7)

The variations in thermocline depth are described by

$$\partial_t h + a_m h + H(\partial_x u + \partial_y v) = 0 \tag{59}$$

The terms describe: the time derivative, frictional damping, and the convergence of currents. Again, advection has been ignored.

The wind stress can be calculated from the wind $\mathbf{U}$ using $\vec{\tau} = \rho_{air} C_D |\mathbf{U}|\mathbf{U}$. Since the model is run in the anomaly mode, one can linearise the wind stres around the background state.

Boundary conditions At the boundaries the flow has to obey:

$$\int_{-\infty}^{\infty} u(0, y, t) dy = 0 \tag{60}$$

(no net mass flow through western boundary,$x = 0$), and

$$u(L, y, t) = 0 \tag{61}$$

(no flow at eastern boundary, $x = L$). In the y direction, where the system is open to the rest of the ocean, all quantities should be bounded.

Surface layer, Ekman dynamics and upwelling In the surface layer, Ekman-like currents are superimposed on the shallow-water dynamics described above. The Ekman currents u_s and v_s are given by

$$a_s u_s - \beta y v_s = \frac{H_2}{H} \frac{\tau_x}{\varrho H_1} \tag{62}$$

$$a_s v_s + \beta y u_s = \frac{H_2}{H} \frac{\tau_y}{\varrho H_1} \tag{63}$$

where the upper equation describes zonal, and the lower meridional momentum balance. The terms describe damping, Coriolis effect, and wind stress. There is no time derivative, that is, the Ekman currents are always in an equilibrium between the wind stress, damping and Coriolis effect. They can be calculated directly from the wind stress.

In case of horizontal convergence in the surface layer ($(\partial_x u_1 + \partial_y v_1) \neq 0$) a vertical velocity is needed to fulfill the continuity equation:

$$w_1 = H_1(\partial_x u_1 + \partial_y v_1) \tag{64}$$

The causing of vertical velocities by horizontal convergence is called upwelling.

Sea surface temperature We assume the surface (Ekman) layer to be well-mixed (eg. by surface waves) and therefore to have a homogeneous temperature (the SST).

The SST is modelled by the following equation:

$$\partial_t T + u_1 \partial_x T + v_1 \partial_y T + a_T(T - T_0) + \frac{M(w_1)}{H_u}(T - T_{sub}(h)) = 0 \tag{65}$$

The terms describe: The time derivative of the SST; advection (for which the velocities in the surface layer, $\mathbf{u}_1$, are relevant); a damping term ('Newtonian cooling') whose effect is to bring the temperature to a background state of radiative equlibrium T_0 (the temperature one would have without ocean dynamics), by effects such as horizontal mixing, transport of sensible/latent heat to the atmosphere, and radiation; and an upwelling term. This term describes the upward transport of cool water from below the surface layer (temperature $T_s(h)$) by the vertical velocities caused by upwelling. $M(\chi) \equiv \mathcal{H}(\chi) \cdot \chi$ where $\mathcal{H}$ is the Heaviside function (physically this implies that temperature change through upwelling only takes place for positive w), H_u is a scale height chosen such as to well represent the temperature gradient.

Since the temperature equation is non-linear, its form changes in the anomaly mode. (It is assumed that the background state in absence of anomalies obeys the model equations). Letting χ be some field, let then

$$\chi = \hat{\chi} + \chi'$$

where $\hat{\chi}$ is the background and χ' the anomaly. The temperature equation then becomes, chosing $T_0 = \hat{T}$,

$$\partial T' + \hat{u}_1 \partial_x T' + u_1' \partial_x (\hat{T}+T') + \hat{v}_1 \partial_y T' + v_1' \partial_y (\hat{T}+T') + a_T T' + [M(\hat{w}_1+w_1') - M(\hat{w}_1)] \cdot \partial_z \hat{T} + \frac{M(\hat{w}_1 + w_1')}{H_u} (\hat{T}+T' - T_{sub}(h)) = 0 \tag{66}$$

In the linear equations, one can simply replace the total quantities by their anomalies. From subsection 4.2 onward, only the anomaly mode will be considered, so the primes indicating the anomalies are omitted in order to keep the notation simpler.

Atmosphere Since we are not interested in a vertical resolution of the atmosphere, it can be described by a shallow-water model. $U$and V denote the zonal and meridional wind, Θ the geopotential. The momentum balances read:

$$(\partial_t U) + a_M U - \beta_0 y V + \partial_x \Theta = 0 \tag{67}$$

$$\partial_t V + a_M V + \beta_0 y U + \partial_y \Theta = 0 \tag{68}$$

where the various terms describe the time derivatives, linearised damping, Coriolis effect, and pressure gradient force.

The geopotential obeys:

$$\partial_t \Theta + a_M \Theta - c_a^2 (\partial_x U + \partial_y V) = -\alpha_T (T - T_0) \tag{69}$$

where the terms describe the time derivative, damping, horizontal convergence, and heating of the atmosphere due to deviations of the SST from radiative equilibrium T_0 (heating causes - via three dimensional circulation processes not resolved in the shallow water model - a decrease in surface pressure/geopotential).

As the atmosphere has little 'memory', compared to the ocean, one can make the approximation that the state of the atmosphere follows instantaneously from the ocean, that is, one omits the time derivatives.

The Cane-Zebiak model allows for the following interactions between its components:

- wind stress: atmosphere transferring momentum to both the oceanic shallow water part and the surface layer (Ekman dynamics).
- temperature advection: the currents in the surface layer ($\vec{u}_1 = \vec{u} + \vec{u}_s$) lead to horizontal temperature advection. This interaction is not linear.
- upwelling: horizontal convergence in the upper layer leads to vertical velocities which, when directed upward, can bring cold water from greater depth (depending on thermocline height) upwards. This interaction is non-linear, too.
- heating: the atmosphere is heated by the ocean (SST), with heating leading to a decrease in geopotential ('pressure'). The heating is linear.

The strength of the coupling between SST and heating is essential for the formation of El Niño's. If it is too weak, then the feedback chain 'SST anomaly → heating → wind stress anomaly → current/thermocline anomaly → SST' will be disrupted and the ENSO dies off. If the coupling is strong enough, however, the ENSO can go on forever without external forcing. Mathematically speaking, there is a Hopf bifurcation in the SST-heating coupling.

The oceanic part of the model allows for two types of waves, eastward travelling equatorial Kelvin waves with a maximum at the equator and slower westwards travelling Rossby waves. Their travel time sets the internal time scale of variability.

4.2 The original Zebiak-Cane Code

I used an existing code of the Zebiak-Cane model into which I implemented the additional DO features. In the following a brief description of the original code will be given before dealing with the DO part. Some minor changes and simplifications made in the original code will also be described. A more detailed description of the model can be found in [Zebiak, Cane 1987]. A few results obtained with this code are given in fig. 16.

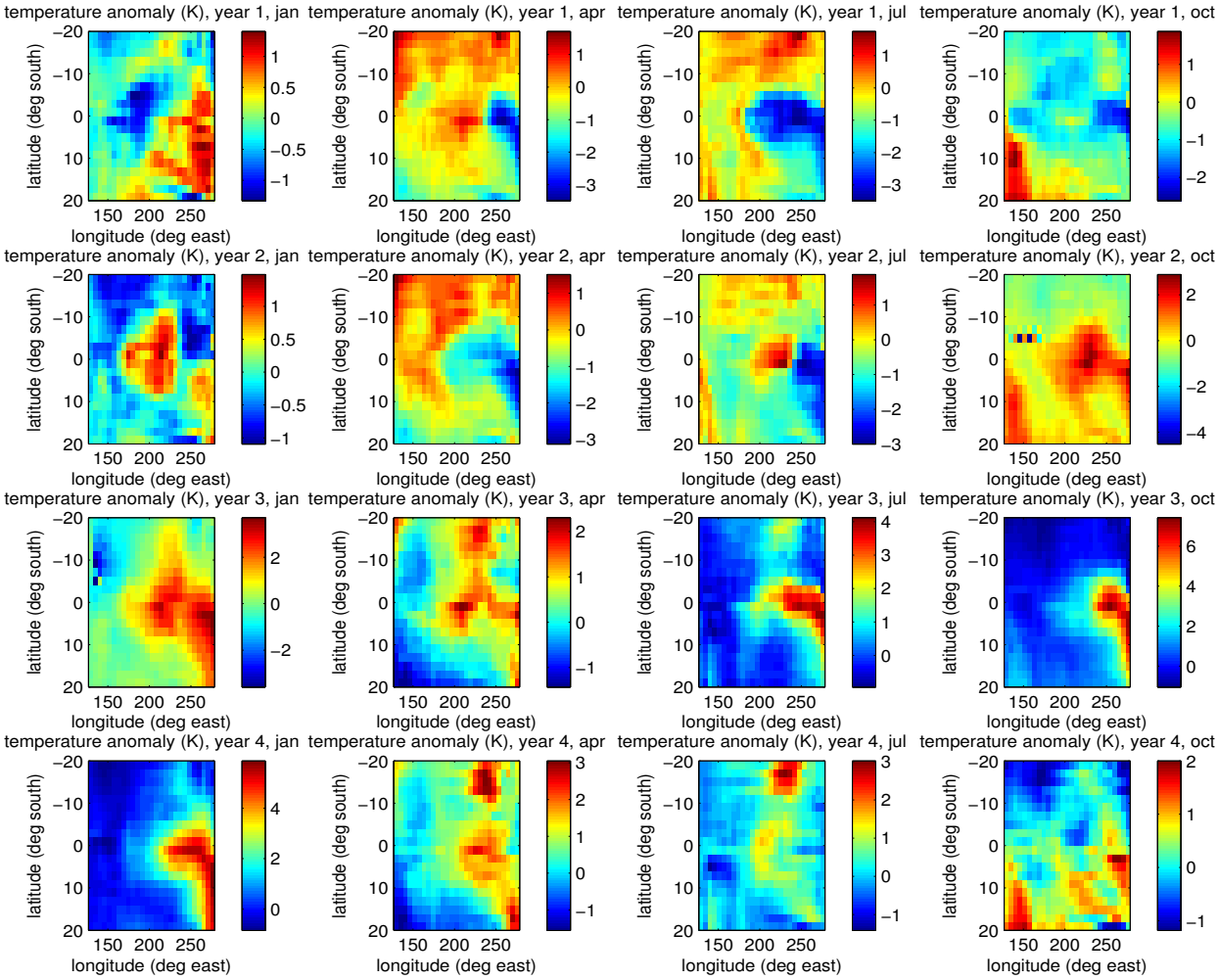

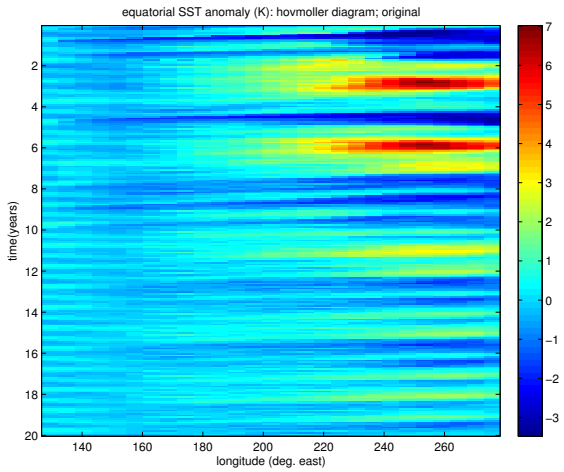

Figure 16: Top: Temperature anomaly of 4 years simulated with the original Zebiak-Cane code, plotted at 3-monthly intervals. There is a La Niña in year 1 and El Niño in year 3-4. The strong asymmetry around the equator near the eastern boundary is caused by the very asymmetric background upwelling.
Bottom: Hovmoller diagram of the temperature anomaly along the equator. The first four years of the Hovmoller plot are those in the top panel. Clearly the ZC code produces very irregular results, with two strong El Niños in the first 10 years, and no strong events in the next 10 years.

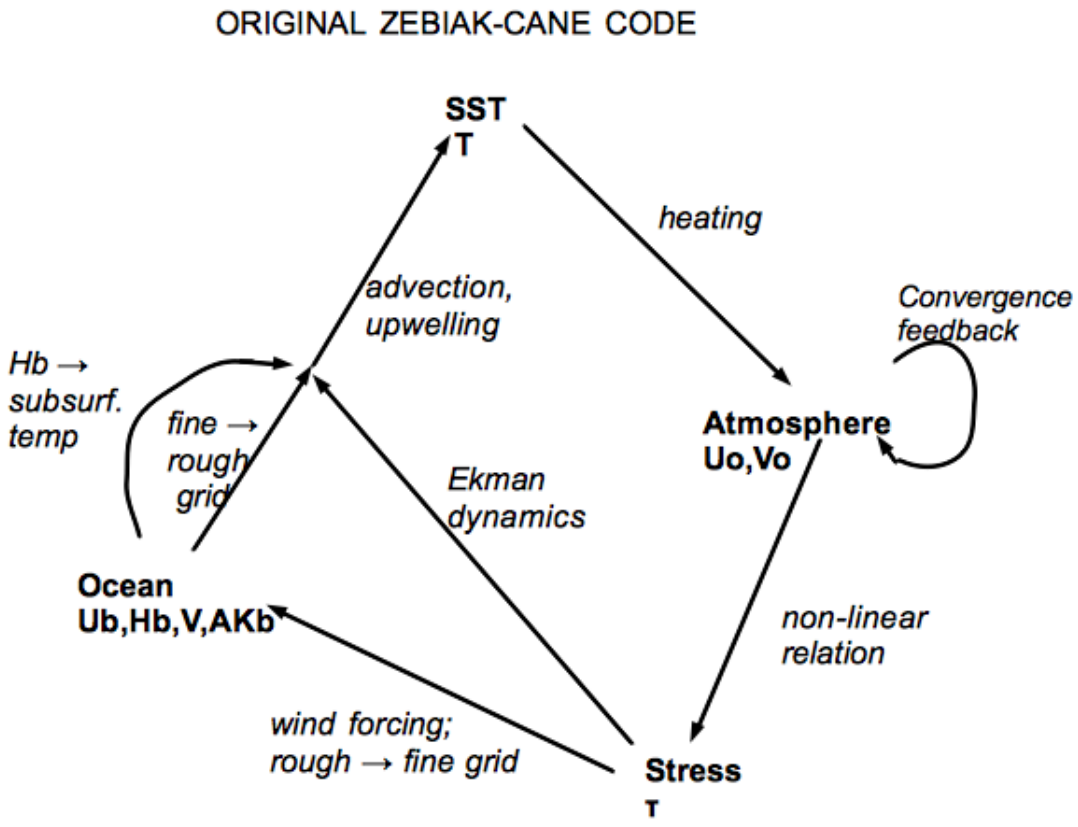

Figure 17: The scheme of the original Zebiak-Cane code. U_o and V_o are the zonal and meridional wind component, τ the wind stress, U_B, H_b, A_{KB}, V the non-Kelvin zonal velocity, non-Kelvin thermocline depth, Kelvin wave amplitude and zonal velocity of the ocean, and T the sea surface temperature.

4.2.1 Description of the code

Discretisation and grids The original code is explicit; the time discretisation resembles an Euler foreward method. During one time step, the code first calculates the temperature changes, then uses the updated temperature to calculate the atmospheric quantities and the wind stress, and finally uses those for updating the oceanic quantities. This use of already updated quantities within one loop is not classically Euler foreward. The scheme of the code is visualised in fig. 17. The time step is set to 10 days (or rather, 1/36 years, where one year consists of 12 equal months) and can unfortunately not be adjusted.

The code operates on two spatial grids. The first one, which will referred to as 'oceanic grid', is for the quantities of the oceanic reduced gravity model, i.e. u, v, h. It is actually a staggered grid with 79 (78) zonal and 115 (116) meridional gridpoints for u and h (v). The other grid is much coarser, with grid cells of 5.625^o in longitude and 2^o in latitude, and covers an area from 29^oS to 29^oN and 129.375^oE to 84.375^oW. It has no staggering. On this grid, all other quantities are specified, such as SST, winds, wind stress, and Ekman related quantities. It will be referred to as 'atmospheric grid'.

Like the time step, grid sizes are not adjustable. The model performs two grid transformations per time step: It computes an ocean-grid wind forcing from the wind stress given on the atmospheric grid, which is used in the reduced gravity model, and it averages the oceanic quantities back onto the coarser atmospheric grid. [6]

SST dynamics After performing spatial averages of the oceanic fields, further quantities have to be calculated: The Ekman velocities are computed from the wind stress, and the upwelling from the divergence of the total velocities in

[6] This averaging was not done neatly, because some oceanic grid points where used for several atmospheric points and hence where given more weight. The staggering of the v grid was not paid attention to, so that a v which is symmetric on the oceanic grid would not remain so on the atmospheric one. I corrected this.

the well-mixed layer. One also needs the subsurface temperature (the temperature at the depth from which water is supposed to be upwelled):

$$T_{sub} = \gamma_{sub} T^*_{sub} + (1 - \gamma_{sub}) T \tag{70}$$

where

$$T^*_{sub} = T_{ai}[tanh(b_i(\hat{h} + h)) - tanh(b_i \hat{h})] \tag{71}$$

with $i = 1$ if $h > 0$ and $i = 2$ if $h < 0$.

The temperature subroutine needs a finer time resolution, hence N_{SST} subtimesteps are taken for this calculation, i.e. one computes the temperature change, divides by N_{SST}, adds the change to the temperature field, and repeats this N_{SST} times. The currents and windstress are not updated in between.

Furthermore, due to some instability, the temperature can become very high at a few locations and times. This is prevented by artificially not letting the total temperature $\hat{T} + T$ rise above 30^oC.

Stress The winds - and hence the wind stress - are determined by heating from the ocean and convection.

In the heating term, $-\alpha_T T$, the coefficient is given a dependence on the background temperature,

$$\alpha_T = \alpha^*_T e^{(\hat{T} - 30^oC)/16.7^O C}$$

The convection loop is non-linear and is supposed to capture the fact that converging winds are linked to rising air, convection, and latent heat release, which again influences the winds. In this project the convection loop is switched off because it is nonlinear and would cause the DO decomposition of atmospheric quantities very complicated.

The atmospheric quantities can either be updated by calculating the changes, or be recalculated completely, based on the temperature. The latter is more costly but the former might lead to a development of unphysical modes. Since the model runs fast enough on modern computers, one can easily choose for recalculation at every time step and hence avoid complicated criteria.

Oceanic quantities The Zebiak-Cane code splits the oceanic zonal velocity and thermocline depth into a Kelvin wave part and a 'rest' part. Since Kelvin waves have a fixed meridional dependence, given by $\phi_K(y)$, one needs to give only the zonal dependence $A_K(x,t)$:

$$\chi_{Kelvin}(x,y,t) = A_K(x,t) * \varphi_K(y) \tag{72}$$

where χ_{Kelvin} stand for the Kelvin-related zonal velocity or thermocline depth (they are equal in the dimensionless system). For the 'rest' part I will use the variables $u_B(x,y,t)$ and $h_B(x,y,t)$. The total zonal velocity and thermocline depth are given as:

$$u(x,y,t) = u_B(x,y,t) + A_K(x,t) * \varphi_K(y) \ ; \ h(x,y,t) = h_B(x,y,t) + A_K(x,t) * \varphi_K(y) \tag{73}$$

where $\varphi_K(y) \propto e^{-y^2/2}$ in non-dimensional units ($y_{dim} = y_{nondim} \times \sqrt{g'H/\beta_0}$).

The Kelvin and 'rest' parts are treated as seperate variables in the oceanic part of the model. For SST dynamics, the sum is used.

Friction is applied in a non-explicite way, namely after updating the oceanic quantities, i.e. after performing calculations including all other processes affecting the oceanic quantities, the result is multiplied with a friction coefficient.

Background Background quantities are all in the atmospheric grid, as they are used for the calculation of the temperature, winds and wind stress (non-linear processes). The following quantities have a background state: zonal, meridional and vertical ocean velocities, SST, zonal and meridional wind, and wind divergence (the latter is not used with the convction being switched off). The background state is season-dependent, with values given for each month; as there are 3 timesteps per month, interpolation is used for the intermediate steps.

For the computation of T_{sub}, a season-independent background thermocline depth is used.

Spin-up and external forcing In the absence of external forcing, it is a solution to have zero anomalies. Hence the model needs either non-zero anomalies as starting condition, or some external forcing for a spin-up. The latter is realised by letting a westerly wind burst around the equator blow for a few months. Once the model is spun-up, it keeps producing El Niños (in an irregular fashion with 3-4 years as preferred period) on its own, i.e. without further external forcing.

parameter	meaning	value	parameter	meaning	value
a_m	oceanic friction	$(2.5\,yr)^{-1}$	g'	reduced gravity parameter	0.0561
a_s	Ekman layer friction	$(2\,days)^{-1}$	a_T	SST damping	$(125\,days)^{-1}$
a_M	atmospheric friction	$(2\,days)^{-1}$	γ	used in T_{sub}	0.75
H	background thermocline depth	150m	T_{a1},T_{a2}	used in T_{sub}	28^oC,-40^oC
H_1	ekman layer deph	50m	b_1,b_2	used in T_{sub}	$1/(80m)$,$1/(33m)$
H_u	depth in vert. SST gradient	$= H_1$	α	SST-heating coupling	$0.031\frac{m^2}{s^3K}$
β	β parameter (Coriolis)				

Table 2: list of most important model parameters

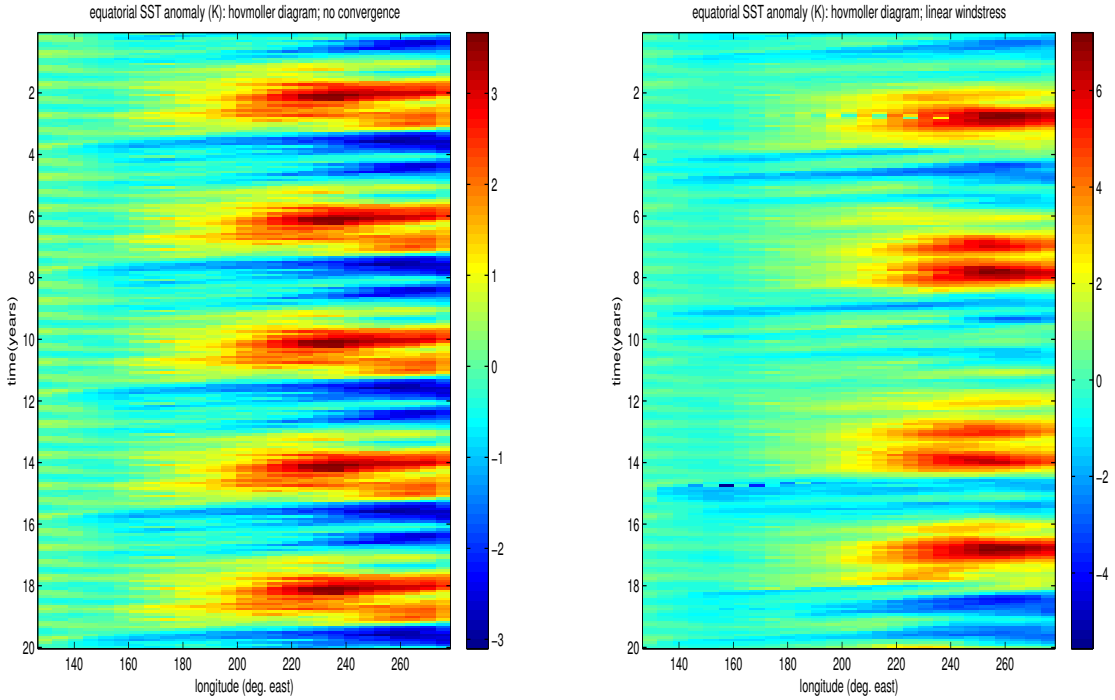

Figure 18: Hovmoller plots of the temperature anomaly along the equator for the modified ZC code. In the left panel, the convergence loop is switched off; in the right panel, the wind stress is linearised. See also fig.16.

4.2.2 Modifications of the ZC code

In oder to implement the DO formalism, it was necessary or handy to make some changes to the original code. The effect of each change on the outcome of the old model was checked. In fig.18 the consequences of these changes are illustrated.

Convergence loop The convergence loop is non-linear and complicates the equations a lot; it would cause difficulties when expanding atmospheric quantities into modes. Furthermore, the computation of this effect involves an iteration with an adaptive number of iteration steps. It would be hard to find a neat way to translate the iteration criterion to modes. Fortunately, the model gives reasonable results without convergence loop, even though the El Niños behave more regularly - in fact, the temperature anomaly becomes almost perfectly periodic, with a period of 4 years (see fig. 18, left), but it still produces El Niño's and La Niña's.

Wind stress The wind stress is also non-linear, while it is desirable to limit non-linearities to the temperature equation. Hence the wind stress

$$\tau_i \propto |\hat{\mathbf{U}} + \mathbf{U}'| \times (\hat{\mathbf{U}} + \mathbf{U}')$$

is linearised around the background state, which gives the wind stress anomaly:

$$\tau_i' \propto (|\hat{\mathbf{U}}| + \frac{\hat{U}_i^2}{|\hat{\mathbf{U}}|})U_i + \frac{\hat{U}_i\hat{U}_k}{|\hat{\mathbf{U}}|}U_k \tag{74}$$

where bold face denotes vectors, and for the indices $(i,k) \in \{(x,y),(y,x)\}$. The prime will be omitted from now on.

Linearising the wind stress also makes El Niño more regular, but not as much as omitting the convergence loop. (see fig. 18, right)

Timestep When applying the DO method, the timestep of 1/3 *month* might be to coarse. It is known that the stochastic coefficients can diverge in case of too large time steps. Unfortunately, the time step size cannot be adjusted in the code. Hence I implemented a substimestep into the whole calculation loop (temperature - wind - stress - ocean): Let N_{loop} be the number of subtimesteps, then the temperature change calculated in the SST-subroutine is divided by N_{loop}. With the updated temperature, the atmospheric quantities and the wind stress are calculated in the usual manner (these are recalculated every time step, based on the temperature field). The change in the oceanic quantities is also divided by N_{loop}. The loop is repeated N_{loop} times within one time step. For the original Zebiak-Cane code, the difference between the solutions with $N_{loop} = 1$ and $N_{loop} = 5$ is far below one procent.

Background seasonal dependence It is usefull to remove the seasonal dependence of the background when wishing to find equilibrated modes (seasonal variation would act as an additional forcing). One can easily run the model with conditions specific for one month, or an annular mean backgrond.

Failed attempts: It was also tried to remove the artificial constraint that the temperature may not exceed 30^oC . This caused occasional spots of very high temperatures. If one doesn't want the ocean to boil, one should not remove this part of the code.

Also my experiments with linearising or smoothening the upwelling (removing the Heaviside function in the upwelling term and using only one function, instead of cases, for the subsurface temperature in eq. 71) gave absurd results.

4.3 DO Equations for ENSO

4.3.1 Aside: diagnostic quantities in the DO formalism

When trying to write down the DO equations for the ZC model, I wondered about how to deal with the meridional velocity, which becomes a diagnostic quantity in the long-wave limit. Recall, the equation for v is

$$\eta\partial_t v + a_m v + \beta_0 y u + g'\partial_y h = \frac{\tau_y}{\rho H}$$

and in the long wave limit, $\eta \to 0$. The meridional momentum equation becomes some algebraic (∂_t-free) constraint on v. For diagmostic quantities one cannot write down a DO equation (one can at most express it via prognostic quantities)

What was puzzling to me were the following questions:

- Can a diagnostic quantity contribute to the metric?
- What happens for small but non-zero η, i.e. is the diagnostic variable case the limit of the prognostic variable case with $\eta \to 0$?

The first question at least is more important for the ocean than the atmosphere, because the atmosphere stores far less energy, and the metric is chosen to be related to the total energy.

The sea surface height in the double gyre system The double gyre system is easier and also contains a diagnostic variable, the sea surface height (SSH) deviation. The total water depth is given by $h_{tot} = H + h$, where $h = \zeta\hat{h}$ is the dimensional and $\hat{h}$ the non-dimensional sea surface height deviation, and H the average water depth (no bottom topography), where ζ is the typical scale of sea surface height deviations. The mean water depth is much larger than the SSH deviation.

Consider the system eq. 26 - 28.

Combining a few coefficients that are not important for the general form into b, c, and α, and writing $\eta = \zeta/H$, the equations can be rewritten as

$$D_t u = fv - b\partial_x(\hat{h}) + c\nabla^2 u + \alpha\tau^x/(H(1+\eta\hat{h})) \tag{75}$$

$$D_t v = -fu - \partial_y(\hat{h}) + c\nabla^2 v + \alpha\tau^y/(H(1+\eta\hat{h})) \tag{76}$$

$$\partial_t(H\eta\hat{h}) + \partial_x(H(1+\eta\hat{h})u) + \partial_y(H(1+\eta\hat{h})v) = 0 \tag{77}$$

Note that η is a small parameter because $H \gg h = \zeta\hat{h}$. In the momentum equations, b is supposed to contain all scaling factors already, so no ζ is appears there.

In the case $\eta \to 0$ (physically: $H \to \infty$), using

$$\partial_t(H\eta\hat{h}) + H\partial_x((1+\eta\hat{h})u) + H\partial_y((1+\eta\hat{h})v) = \eta[\partial_t\hat{h} + \partial_x(\hat{h}u) + \partial_y(\hat{h}v)] + \partial_x u + \partial_y v$$

the equations become

$$D_t u = fv - b\partial_x(\hat{h}) + c\nabla^2 u + \alpha\tau^x/H \tag{78}$$

$$D_t v = -fu - \partial_y(\hat{h}) + c\nabla^2 v + \alpha\tau^y/H \tag{79}$$

$$\partial_x u + \partial_y v = 0 \tag{80}$$

The question is, what happens when writing down the DO equations for the first set of equations and taking the limit afterwards?

One can write down the DO equations for this system easily (just insert into the general DO equations), apart from the fact that the metric is not a priori known. Let $\phi = (u, v, \hat{h})^T$, and $\phi^2 = (u, v)^T$. The inner product in first case is $< \phi^2, \chi^2 >= \int_V \phi(x,y)^2_{,a} A_{ab} \chi^2_b(x,y) dxdy$ where the indices a, b denote components of the field vector. The metric is of the form $A = \begin{pmatrix} 1/2 & 0 \\ 0 & 1/2 \end{pmatrix}$ (see eq. 39, except that a trivial factor 1/2 is introduced here because the inner product then resembles the kinetic energy better). The same formulation can be applied to $\phi = (u, v, \hat{h})^T$, where I leave the form of the metric undetermined at first:

$$< \phi, \chi >= \int_V \phi(x,y)_{,a} A_{ab} \chi_b(x,y) dxdy$$

with

$$A = \begin{pmatrix} 1/2 & 0 & A_{uh} \\ 0 & 1/2 & A_{vh} \\ A_{uh} & A_{vh} & A_{hh} \end{pmatrix}$$

The equations for the DO modes illustrate best what happens when taking the infinite waterdepth limit.

In the case of $\eta \neq 0$, one can expand $\hat{h} = \bar{\hat{h}} + Y_i \hat{h}_i$. If $\eta = 0$ one has to use expansions similar to those given in eqs. 45-47. Within the momentum equations, I will leave $\hat{h}$ unexpanded. I will also insert the stochastic forcing, $F = (F_u, F_v, \eta F_h)$ and $F^2 = (F_u, F_h)$. The scaling of the F_h with η is a requirement, not derived from something.

With

$$B_j \equiv E^\omega[(\mathcal{L}(\phi) + F)Y_j]$$

(B has 3 components, for $u, v, \hat{h}$) and

$$I_{jl} \equiv < B_j, \phi_l >= \int_V B_j A \phi_l dxdy$$

the DO equations become

$$\partial_t u_i = (B_j)_u C^{-1}_{ij} - I_{jl} C^{-1}_{ij} u_l \tag{81}$$

$$\partial_t v_i = (B_j)_v C^{-1}_{ij} - I_{jl} C^{-1}_{ij} v_l \tag{82}$$

$$\partial_t \hat{h}_i = (B_j)_h C^{-1}_{ij} - I_{jl} C^{-1}_{ij} \hat{h}_l \tag{83}$$

B_j is given by:

$$B_j = \begin{pmatrix} \{(-\overline{u}\partial_x u_k - u_k \partial_x \overline{u} - \overline{v}\partial_y u_k - v_k \partial_y \overline{u} + f v_k + c \triangle u_k) C_{kj} \\ +(-u_j \partial_x u_k - v_j \partial_y v_k) C_{lkj} + E^\omega[(-b\partial_x \hat{h} + \frac{\alpha \tau^x}{H(1+\eta\hat{h})} + F_u) Y_j]\} \\ \\ \{(-\overline{v}\partial_y v_k - v_k \partial_y \overline{v} - \overline{u}\partial_x v_k - u_k \partial_x \overline{v} - f u_k + c \triangle u_k) C_{kj} \\ +(-v_j \partial_y v_k - u_j \partial_x u_k) C_{lkj} + E^\omega[(-b\partial_y \hat{h} + \frac{\alpha \tau^y}{H(1+\eta\hat{h})} F_v) Y_j]\} \\ \\ \{(-(H/\eta + \overline{\hat{h}})\nabla \cdot u_k - \hat{h}_k \nabla \cdot \overline{u} - \overline{u} \cdot \nabla \hat{h}_k - u_k \cdot \nabla \overline{\hat{h}}) C_{kj} \\ +(-\hat{h}_k \nabla \cdot u_l - u_l \cdot \nabla \hat{h}_k) C_{lkj} + E^\omega[F_p Y_j]\} \end{pmatrix} \tag{84}$$

inserting the DO expansions for u and v and using $E^\omega[\overline{\chi} Y_j] = 0$ for any quantity χ, and $E^\omega[Y_j Y_k Y_l ...] \equiv C_{jkl...}$

When taking $\eta = 0$ before writing the DO equations, one obtains

$$\partial_t u_i = (B^2_j)_u C^{-1}_{ij} - I^2_{jl} C^{-1}_{ij} u_l \tag{85}$$

$$\partial_t v_i = (B^2_j)_v C^{-1}_{ij} - I^2_{jl} C^{-1}_{ij} v_l \tag{86}$$

and the constraint $\nabla \cdot \mathbf{u} = 0$ which leads to $\nabla \cdot \bar{\mathbf{u}} = 0$ by taking the mean of the equation, and $\nabla \cdot \mathbf{u_i} = 0$ applying

$$0 = C^{-1}_{ij} E^\omega[Y_j(\nabla \cdot \mathbf{u})] = C^{-1}_{ij} E^\omega[Y_j(\nabla \cdot \bar{\mathbf{u}} + Y_k \mathbf{u}_k)] = C^{-1}_{ij} C_{jk} (\nabla \cdot \mathbf{u}_k) = \nabla \cdot \mathbf{u}_i$$

B^2_j is defined as

$$B^2_j = \begin{pmatrix} \{(-\overline{u}\partial_x u_k - u_k \partial_x \overline{u} - \overline{v}\partial_y u_k - v_k \partial_y \overline{u} + f v_k + c \triangle u_k) C_{kj} \\ +(-u_j \partial_x u_k - v_j \partial_y v_k) C_{lkj} + E^\omega[(-b\partial_x \hat{h} + \frac{\alpha \tau^x}{H} + F_u) Y_j]\} \\ \\ \{(-\overline{v}\partial_y v_k - v_k \partial_y \overline{v} - \overline{u}\partial_x v_k - u_k \partial_x \overline{v} - f u_k + c \triangle u_k) C_{kj} \\ +(-v_j \partial_y v_k - u_j \partial_x u_k) C_{lkj} + E^\omega[(-b\partial_y \hat{h} + \frac{\alpha \tau^y}{H} F_v) Y_j]\} \end{pmatrix} \tag{87}$$

When taking $\eta = 0$ in the three-component system, the equations for u and v take the same form as in the two-component system, but the I_{jl} - term might take different values. The last equation, when considering only terms to leading order in η i.e. $(\mathcal{O}(\eta^{-1}))$, becomes

$$\nabla \cdot \mathbf{u}_i - \int_V \nabla \cdot u_i [A_{uh} u_l + A_{vh} v_l + A_{hh} \hat{h}_l] \hat{h}_l + \mathcal{O}(\eta) = 0$$

If now the metric components containing h are all at most $\mathcal{O}(\eta)$, then one obtains $\nabla \cdot \mathbf{u}_i = 0$ to leading order. This maens that all terms in $(B_j)_h$ are $\mathcal{O}(\eta^0)$ and hence with the corresponding metric components A_{uh}, A_{vh}, A_{hh} being $\mathcal{O}(\eta^1)$, the $\hat{h}$ equation does not contribute to I_{jl} anymore and thus the two cases become equivalent.

Energy density for the double gyre The inner product should give the energy. Furthermore, the energy density should fulfill

$$\partial_t e + \nabla \cdot (\mathbf{u}(e + K)) = 0 \tag{88}$$

for arbitrary scalar K. (Here $\mathbf{u}$ and ∇ are two-dimensional!). With suitable boundary conditions, like no flow through the boundary, the energy is then conserved:

$$\frac{dE}{dt} \equiv \int_V \partial_t e \, dxdy = -\int_V \nabla \bullet (u(e + K)) \, dxdy = 0 \;\; (suitable\, bc.) \tag{89}$$

One can easily check that $e_{kin} = \frac{H}{2}(u^2 + v^2)$ fulfills this condition in the $\eta = 0$ case, in absence of friction and forcing. For $\eta \neq 0$, one needs to take potential energy into account, and the energy density becomes

$$e = e_{kin} + e_{pot} = \frac{H(1 + \eta\hat{h})}{2}(u^2 + v^2) + \frac{b}{2}(H\eta\hat{h})^2$$

Dividing by H and remembering that $\eta = \zeta/H$, where ζ is finite, one obtains

$$e = \frac{1+\eta\hat{h}}{2}(u^2+v^2) + \frac{b}{2}\zeta\eta\hat{h}^2$$

so the potential part is $\mathcal{O}(\eta)$.

The metric then is

$$A_{gyre} = \begin{pmatrix} 1/2 & 0 & 0 \\ 0 & 1/2 & 0 \\ 0 & 0 & b\zeta\eta/2 \end{pmatrix} \tag{90}$$

Mechanical energy density for ENSO For ENSO, there is an oceanic diagnostic quantity, v. As in the gyre case, this could lead to inconsistencies except if the v-components of the metric vanish in the long-wave limit. In order to show that this is the case, one can derive the mechanical energy density in the reduced gavity model, and then take te limit.

Consider the oceanic momentum and continunity equations 57-59, removing terms that obviously do not conserve the energy of this subsystem (friction, wind stress), but taking into account advection (which is actually neglected in the model because it is non-linear). This leads to

$$\partial_t u + \mathbf{u}\cdot\nabla u - \beta y v + g'\partial_x h = 0 \tag{91}$$

$$\eta(\partial_t u + \mathbf{u}\cdot\nabla v) + \beta y v + g'\partial_y h = 0 \tag{92}$$

$$\partial_t h + \mathbf{u}\cdot\nabla h + h\nabla\cdot\mathbf{u} = 0 \tag{93}$$

Now consider the sum

$$hu \times [\text{zonal momentum eq}] + hv \times [\text{meridional momentum eq}] + (u^2+\eta v^2)/2 \times [\text{continuity eq}] \tag{94}$$

which yields

$$\partial_t e_{kin} + \nabla\cdot(u e_{kin}) + g' h u\cdot\nabla h = 0 \tag{95}$$

with $e_{kin} = \frac{h}{2}(u^2+\eta v^2)$.The last term in eq.95 can be rewritten, using continuity in the second step:

$$g' h\mathbf{u}\cdot\nabla h = g'\nabla\cdot(\mathbf{u}h^2) - g' h\nabla\cdot(\mathbf{u}h) = g'\nabla\cdot(\mathbf{u}h^2) + \frac{g'}{2}\partial_t h^2 \tag{96}$$

Inserting this into eq.95 yields:

$$\partial_t e_{ocean} + \nabla\cdot(\mathbf{u}e_{ocean}) + \frac{g'}{2}\nabla\cdot(\mathbf{u}h^2) = 0 \tag{97}$$

with the mechanical (kinetic plus potential) mechanic energy $e_{ocean} \equiv e_{kin} + \frac{g'}{2}h^2 = \frac{h}{2}(u^2+\eta v^2) + \frac{g'}{2}h^2$. Clearly e_{ocean} fullfills the energy conservation condition, eq.88 so it is really a conserved energy density. Therefore the contribution of the mechanical energy to the metric is

$$A_{mech} = \begin{pmatrix} \frac{h}{2} & 0 & 0 \\ 0 & \frac{\eta h}{2} & 0 \\ 0 & 0 & \frac{g'}{2} \end{pmatrix} \tag{98}$$

with the scalar product $<\varphi_1,\varphi_2> = \int (u_1,v_1,h_1)A_{ocean}(u_2,v_2,h_2)^T dx$. When taking $\eta = 0$, one can simply take v out of the inner product altogether.

4.3.2 The metric for ENSO

The atmosphere is considered not to contribute to the energy density because of its small density and heat capacity, and v does not contribute either, but the SST certainly does.

There is no obvious choice - from a physical point of view - for an expression for the thermal energy. (Ideally one would have a formulation which filters out the part of the thermal energy that can be converted into mechanic energy, and which depends on the SST.) So a mathematically simple choice is made, namely $e_{therm} = CT^2$; $C > 0$ The advantage of this formulation is that it is positive definite, and fits naturally into an inner product. C is some coefficient whose numerical value has to be determined in such a way as to obtain modes which make sense - that is, involve both temperature and mechanical quantities in some weighed manner (see subsection 4.4.1). (Unfortunately we do not have a main balance, equivalent to, say, geostrophic balance in other systems, to which we can tune C.)

Wishing the metric to be time-independent, the factor h in the first metric component is replaced by the typical thermocline depth scale, H.

The complete metric now reads:

$$A = \begin{pmatrix} \frac{H}{2} & 0 & 0 \\ 0 & \frac{g'}{2} & 0 \\ 0 & 0 & C \end{pmatrix} \tag{99}$$

with the scalar product

$$< \varphi_1, \varphi_2 >= \int (u_1, h_1, T_1) A (u_2, h_2, T_2)^T dx \tag{100}$$

4.3.3 DO equations for ENSO

The prognostic quantities u, h, T [7]can be decomposed in mean and modes immediately: $u = \bar{u} + Y_i u_i$ etc: but the expansion of other quantities depends on the expansion of these three fields. Fortunately, after the linearisations/simplifications described in 4.2.2, v, u_s, v_s, Θ, U, V all depend on the other quantities linearly, hence they can be decomposed in the same way: $U = \bar{U} + Y_i U_i$ etc.

The windstress anomaly is still given by

$$\tau_x \propto (|\hat{\mathbf{U}}| + \frac{\hat{U}^2}{|\hat{\mathbf{U}}|})U + \frac{\hat{U}\hat{V}}{|\tilde{\mathbf{U}}|}V \ , \ \tau_y \propto (|\hat{\mathbf{U}}| + \frac{\hat{V}^2}{|\hat{\mathbf{U}}|})V + \frac{\hat{U}\hat{V}}{|\hat{\mathbf{U}}|}U$$

Mean The linear equations remain in their original form:

$$\partial_t \bar{u} + a_m \bar{u} - \beta_0 y \bar{v} + g' \partial_x \bar{h} = \frac{\bar{\tau_x}}{\rho H} \tag{101}$$

$$a_m \bar{v} + \beta_0 y \bar{u} + g' \partial_y \bar{h} = \frac{\bar{\tau}_y}{\rho H} \tag{102}$$

$$\partial_t \bar{h} + a_m \bar{h} + H(\partial_x \bar{u} + \partial_y \bar{v}) = 0 \tag{103}$$

The Ekman layer equations become

$$a_s \bar{u}_s - \beta y \bar{v}_s = \frac{H_2}{H} \frac{\bar{\tau}_x}{\varrho H_1} \tag{104}$$

$$a_s \bar{v}_s + \beta y \bar{u}_s = \frac{H_2}{H} \frac{\bar{\tau}_y}{\varrho H_1} \tag{105}$$

For the temperaure, I define

$$A_{upwell}(\omega) = [M(\hat{w}_1 + w_1(\omega)) - M(\hat{w}_1)] \cdot \partial_z \tilde{T} + \frac{M(\hat{w}_1 + w_1(\omega))}{H_u}(T(\omega) - T_{sub}(h(\omega)))$$

With this, the mean temperature evolves as

$$\partial_t \bar{T} + a_T \bar{T} + E^\omega[A_{upwell}] + E^\omega[(u_1 + \hat{u}_1)\partial_x T + (v_1 + \hat{v}_1)\partial_y T] + \bar{u}_1 \partial_x \tilde{T} + \bar{v}_1 \partial_y \tilde{T} = 0 \tag{106}$$

[7]In the code of the ZCmodel, there are four prognostic quantities, because the Kelvin wave amplitude is treated seperately. This willbe described this in the next section, beause here I want to keep things independent of the implementation.

and the atmospheric equations become

$$a_M \bar{U} - \beta_0 y \bar{V} + \partial_x \bar{\Theta} = 0 \tag{107}$$

$$a_M \bar{V} + \beta_0 y \bar{U} + \partial_y \bar{\Theta} = 0 \tag{108}$$

$$a_M \bar{\Theta} - c_a^2 (\partial_x \bar{U} + \partial_y \bar{V}) = -\alpha_T (\bar{T} - T_0) \tag{109}$$

The stochastic forcing does not appear in the mean equations, because it is zero-mean (this means that one has to make it realisation-dependent or zero).

DO modes Here one can make use of the fact that

$$E^\omega[\chi_k Y_k(\omega) Y_j(\omega)] C_{ij}^{-1} = \chi_i \ \ \forall \chi i$$

Defining $I_{jl} =< B_j, \varphi_l >$ with

$$B_j = \begin{pmatrix} -a_m u_j + \beta_0 y v_j - g' \partial_x h_j + \frac{\tau_{j,x}}{\rho H} + E^\omega[F_u(\omega) Y_k(\omega)] C_{jk}^{-1} \\ -a_m h_j - H(\partial_x u_j + \partial_y v_j) + E^\omega[F_h(\omega) Y_k(\omega)] C_{jk}^{-1} \\ -\hat{u}_1 \partial_x T_j - \hat{v}_1 \partial_y T_j - a_T T_j + E^\omega[\{u(\omega)_1 \partial_x (\hat{T} + T(\omega)) - v_1(\omega) \partial_y (\hat{T} + T(\omega)) - A_{upwell}(\omega) + F_T(\omega)\} Y_k(\omega)] C_{jk}^{-1} \end{pmatrix}$$

With this, the evolution of the DO modes can be formulated:

$$\partial_t u_i = -a_m u_i + \beta_0 y v_i - g' \partial_x h_i + \frac{\tau_{i,x}}{\rho H} + E^\omega[F_u(\omega) Y_k(\omega)] C_{ik}^{-1} - I_{il} u_l \tag{110}$$

$$0 = -a_m v_i - \beta_0 y u_i - g' \partial_y h_i + \frac{\tau_{i,y}}{\rho H} + E^\omega[F_v(\omega) Y_k(\omega)] C_{ik}^{-1} \tag{111}$$

$$\partial_t h_i = -a_m h_i - H(\partial_x u_i + \partial_y v_i) + E^\omega[F_h(\omega) Y_k(\omega)] C_{ik}^{-1} - I_{il} h_l \tag{112}$$

The temperature modes follow

$$\partial_t T_i = -\hat{u}_1 \partial_x T_j - \hat{v}_1 \partial_y T_j - a_T T_j + E^\omega[\{u(\omega)_1 \partial_x (\hat{T} + T(\omega)) - v_1(\omega) \partial_y (\hat{T} + T(\omega)) - A_{upwell}(\omega) + F_T(\omega)\} Y_k(\omega)] C_{ik}^{-1} - I_{il} T_l \tag{113}$$

The Ekman and atmospheric equations keep their form also in case of the modes:

$$a_M U_i - \beta_0 y V_i + \partial_x \Theta_i = 0 \tag{114}$$

$$a_M V_i + \beta_0 y U_i + \partial_y \Theta_i = 0 \tag{115}$$

$$a_M \Theta_i - c_a^2 (\partial_x U_i + \partial_y V_i) = -\alpha_T T_i \tag{116}$$

In the last equation, the term $\alpha_T T_0$ is dropped because $E^\omega[T_0] - T_0 = 0$.

Stochastic coefficients The stochastic coefficients change according to

$$dY_i(\omega)/dt = \\ < (1 - E^\omega) \begin{pmatrix} -a_m u(\omega) + \beta_0 y v(\omega) - g' \partial_x h(\omega) + \frac{\tau_{j,x(\omega)}}{\rho H} + F_u(\omega) \\ -a_m h(\omega) - H(\partial_x u(\omega) + \partial_y v(\omega)) + F_h(\omega) \\ -\hat{u}_1 \partial_x T(\omega) - \hat{v}_1 \partial_y T_{(\omega)} - a_T T_{(\omega)} + u(\omega)_1 \partial_x (\hat{T} + T(\omega)) - v_1(\omega) \partial_y (\hat{T} + T(\omega)) - A_{upwell}(\omega) + F_T(\omega) \end{pmatrix} , \begin{pmatrix} u_i \\ h_i \\ T_i \end{pmatrix} > \tag{117}$$

Initial conditions The initial modes are the eigenvector of the covariance operator, which in case of a trivial metric (proportional to unity matrix) reads

$$C_{\varphi(.,t_0,\omega),\varphi(.,t_0,\omega)}(\mathbf{x_1},\mathbf{x_2}) = E^{\omega}[\widetilde{\varphi}(\mathbf{x_1}t_0,\omega) \otimes_{ab} \widetilde{\varphi}(\mathbf{x_2},t_0,\omega)] \tag{118}$$

where φ are N_{real} possible initial realisations and $\tilde{\varphi}(\omega) = \varphi(\omega) - \bar{\varphi}$ and $\otimes_{ab}$ denotes the tensor product in the field component space (the indices a, b stand for the field components u, h, T).

In case of a non-trivial metric, a complication arises which is not considered in [Sapsis, Lermusiaux 2009]. The modes are supposed to be orthonormal with respect to the metric, i.e.

$$< \varphi_i, \psi_j > \equiv \int_V \varphi_{i,a}(x,y)\, A_{ab} \psi_{j,b}(x,y) = \delta_{ij}$$

where δ_{ij} is the Kronecker delta. However, the $C_{\varphi(.,t_0,\omega),\varphi(.,t_0,\omega)}(\mathbf{x_1},\mathbf{x_2})$ that is given above is symmetric (in the combined field component and spatial space) and positive definite, and hence its eigenvectors are orthonormal with respect to the unity metric.

The problem can be solved by using the Cholesky decomposition of the metric. (Any symmetric positive definite matrix A, such as the metric, can be written as $A = LL^T$, where L is a lower triangular matrix.) The first step is to multiply φ by L^T prior to computing $C_{\varphi\varphi}$. This yields

$$\begin{aligned} \hat{C}_{\varphi(.,t_0,\omega),\varphi(.,t_0,\omega)}(\mathbf{x_1},\mathbf{x_2}) &= E^{\omega}[L^T\widetilde{\varphi}(\mathbf{x_1}t_0,\omega) \otimes_{ab} L^T\widetilde{\varphi}(\mathbf{x_2},t_0,\omega)] \\ &= E^{\omega}[L^T\widetilde{\varphi}(\mathbf{x_1}t_0,\omega)\, \widetilde{\varphi}^T(\mathbf{x_1}t_0,\omega)L] = L^T C_{\varphi(.,t_0,\omega),\varphi(.,t_0,\omega)}(\mathbf{x_1},\mathbf{x_2})\, L \end{aligned}$$

This has also the advantage that $C_{\varphi\varphi}$ has the same dimensions in each component.

$\hat{C}_{\varphi\varphi}$ is still symmetric positive definite, hence any two eigenvectors v_i, v_j are orthonormal with respect to the standard inner product: $< v_i, v_j >_{STD} \equiv \int_V \varphi_{i,a}(x,y)\, \mathbb{I}_{ab} \psi_{j,b}(x,y) = \delta_{ij}$ with the identity matrix $\mathbb{I}$. Now consider

$$< v_i, v_j >_{STD} = < v_i, L^{-1}LL^T L^{T-1} v_j >_{STD} = < L^{T-1}v_i, AL^{T-1}v_j >_{STD} = < L^{T-1}v_i, L^{T-1}v_j >$$

Since v_i is an eigenvector of $\hat{C}_{\varphi\varphi}$, $L^{T-1}v_i$ is an eigenvector of $L^{T-1}\hat{C}_{\varphi\varphi}L^T = C_{\varphi\varphi}LL^T = C_{\varphi\varphi}A$.

The covariance operator in case of a non-trivial metric A is thus

$$C^A_{\varphi(.,t_0,\omega),\varphi(.,t_0,\omega)}(\mathbf{x_1},\mathbf{x_2}) = E^{\omega}[\widetilde{\varphi}(\mathbf{x_1}t_0,\omega) \otimes_{ab} \widetilde{\varphi}(\mathbf{x_2},t_0,\omega)]A$$

4.4 Implementing DO Evolution into the Zebiak-Cane model

The model is rewritten, using the subroutines of the original version whenever possible, in such a way as to perform a DO analysis of the ENSO system. The maximal number of modes is 10, the maximal number of realisations is 10000.

4.4.1 The inner product

Numerical values of the metric coefficients The metric has 3 non-zero components. It is always possible to rescale the metric by a scalar factor S^2 (the modes are than rescaled by $1/S$). Furthermore, the coefficient C for the thermal energy is not known. Hence all that is given is the ratio between A_{uu} and A_{hh}, which is $A_{hh}/A_{uu} = g'/H \equiv b = 3.75 \times 10^{-4} s^{-2}$ (see also eq. 99).The metric can then be written as

$$A = \begin{pmatrix} a & 0 & 0 \\ 0 & ab & 0 \\ 0 & 0 & c \end{pmatrix}$$

with two unknowns, a and c.

With the notation $S_\chi = \frac{1}{V}\int_V \chi^2 dxdy$ [8] the square of the norm of $\phi = (u, h, T)$ can be written as

$$< \phi, \phi > = aS_u + abS_h + cS_T$$

Typical values for the S_χ can be determined using the original ZC code.

Now a and c are chosen such that

[8] in the discrete case: $\frac{1}{N_{grid}} \sum_{grid\, points} \chi^2$

- for typical S_u, S_h, S_T the thermal contribution to the innerproduct is as large as the kinetic one, $cS_T = a(S_u + bS_h)$
- for typical S_u, S_h, S_T the norm is 1. Since modes have norm 1 in the DO formalism, this ensures that the modes have reasonable magnitues.

With $S_u = 0.0223(m/s)^2$, $S_h = 626m^2$, and $S_T = 0.877K^2$ the first requirement leads to

$$c/a = (S_u + bS_h)/S_T = 0.2929(\frac{m}{sK})^2$$

and the second to

$$a = 1.946(m/s)^2$$

The metric is:

$$A = \begin{pmatrix} 1.946(s/m)^2 & 0 & 0 \\ 0 & 7.29 \times 10^{-4} m^{-2} & 0 \\ 0 & 0 & 0.5701K^{-2} \end{pmatrix} \tag{119}$$

The code calculates a half-nondimesionalised unit system, giving temperatures in K, thermocline heights in m, and currents in $2cm/s$. In these units, $A_{uu} = 7.784 \times 10^{-4}(s/2cm)^2$ (almost the same value as A_{hh}).

The discretised version of the inner product Let N_A be the number of atmospheric grid points and N_O the number of oceanic grid points. The grid points can be given two indices i_x and i_y for each spatial direction, or one collective index i ($i = (i_y - 1)N_x + i_x$). The inner product then becomes

$$< \varphi_1, \varphi_2 >= \frac{1}{N_O} \sum_{i=1}^{N_O} A_{uu} u_1(i) u_2(i) + A_{hh} h_1(i) h_2(i) \; + \; \frac{1}{N_A} \sum_{i=1}^{N_A} A_{TT} T_1(i) T_2(i) \tag{120}$$

4.4.2 Time evolution

The existing parts of the code have to be modified such as to compute mode and mean, and new subroutines have to be written for performing the projection of the change in the mode onto the space perpendicular to the modes, and for computing the stochastic coefficients and the forcing.

The new code first calculates the temperature change and the atmospheric quantities and wind stress, then the stochastic forcing and the change in the oceanic grid-quantities. Next, the changes in the prognostic quantities are projected to the space perpendicular to the modes. Finally, the stochastic coefficients and covariance matrix and its inverse are computed.

The background states are not season-dependent here, in order to avoid additional time-dependent forcing. Instead, an average is taken over all 12 months.

Temperature change As in the original version, the deterministic temperature change (i.e. not including stochastic forcing) is calculated first. This has do be done realisationwise, because the upwelling term cannot be expanded as a finite powerseries in Y. So rather than using an equation of the form

$$\partial_t T_i = A + B\varphi_i Y_i + C\varphi_i Y_i \varphi_j Y_j + ...$$

(as is done in the double gyre system), one has to express all fields that contribute to the temperature in realisations, $\varphi(\omega) = \bar{\varphi} + Y_i \varphi_i$.

The temperature check (total temperatures above 30^oC are put to 30^oC) also has to be done realisationwise. Averaging over the realisationwise temperature change contributions $\mathcal{L}_T(\varphi)$ [9] gives the change of the mean, and the changes of the modes are obtained applying $E^\omega[\mathcal{L}_T(\varphi)Y_j]C_{ij}^{-1}$. The realisationwise contributions are saved for the computation of the stochastic coefficients.

Atmosphere, wind stress, and ocean Due to the linearity of these processes, all necessary quantities are expressed in mean and modes, and all calculations can be done as in the old code, except that they are performed $N_{mode} + 1$ times, namely once for each of the N_{mode} modes en once for the mean.

[9] $\mathcal{L}_T(\varphi)$ is not the realisationwise temperature change but the realisationwise result of applying the operator $\mathcal{L}$. The temperature change of a realisation is given by $d\bar{T} + Y_i dT_i$.

Stochastic forcing The spatial pattern $F_S = (F_{S,u}, F_{S,h}, ...)$ of the stochastic forcing is an external input. For example, one can force the original model for 1-2 months with a wind burst and take the solutions for u_B, v, h_B, A_K, T after this time as spatial pattern (up to a scaling factor). [10]

A Gaussian-distributed random number $W(\omega)$ (in case of white noise) or $\eta(\omega)$ with

$$d\eta(t) = -\frac{1}{\tau}\eta(t)\,dt + \sqrt{2/\tau}\,dW(t)$$

(red noise) is multiplied with the spatial pattern to give the (realisationwise) stochastic forcing.

The realisationwise forcing is converted into modewise forcing using $F_i = E^\omega[Y_j(\omega)F_S(\omega)]C_{ij}^{-1}$. The modewise forcing is added to u_B, v, h_B, A_K, T.

Projection The solutions for u_B, v, h_B, A_K, T form the end of the previous time step have been saved ($u_{B,old}$ etc), so that the change $du_B \equiv u_B - u_{B,old}$ can be calculated. With

$$\varphi(x.y) = (u_B(x,y) + \phi_K(y)A_K(x), h_B(x,y) + \phi_K(y)A_K(x), T(x,y))$$

and $\chi \in \{u_B, v, h_B, A_K, T\}$, the projection is:

$$\chi_i \to \chi_i - < d\varphi_i, \varphi_{old,j} > \chi_{oud,j}$$

Note that v, despite not being a prognostic quantity and hence not appearing in the innerproduct, also undergoes projection. Otherwise, (u_B, v, h_B, A_K, T) would not form a solution anymore.[11]

In principle, the projection should be sufficient to keep the modes orthonomal, but in practice, they can become more and more parallel due to numerical errors. Therefore a Gram-Schmidt orthonormalisation of the modes is performed after the projection. The mode which has currently the second largest variance ($E^\omega[Y_i^2(\omega)]$) is projected onto the space orthogonal to the mode with the largest variance, the third largest mode is made orthogonal to these two, and so on. This way, the most important modes are manipulated least. Again, even though v does not contribute to the innerproduct, it undergoes the same projections as the other quantities.

The last thing to do is to save the modes as $\cdot_{old}$ for use in the next time step.

Stochastic coefficients and covariance matrix The coefficients are computed by calculating the contributions from stochastic noise, and deterministic parts of temperature and oceanic field changes seperately.

The stochastic forcing part yields $[dY_i(\omega)]_{stoch} < F_S W(\omega), \varphi_i >$. The deterministic temperature part yields

$$[dY_i(\omega)]_T = < (0, 0, \mathcal{L}_T(\phi(\omega))), \varphi_i >$$

the $\mathcal{L}_T(\varphi)$ have been saved from the temperature calculation. The mean of these contributions is substracted. Due to linearity, the oceanic quantities u and h fulfill $\mathcal{L}(u(\omega)) = \mathcal{L}\bar{u} + Y_i\mathcal{L}(u_i)$. Hence one can write the deterministic oceanic contribution as

$$[dY_i(\omega)]_{u,h} < (\mathcal{L}_u(\phi_j), \mathcal{L}_h(\phi_j), 0), \varphi_i > Y_j(\omega)$$

which is already zero-mean. (One could also first construct the $\mathcal{L}(u(\omega))$ but the other formulation is a bit faster to compute).

Adding up these changes to the old coefficients yield the new ones.

Now one calculates the variance matrix $C_{ij} = E^\omega[Y_i(\omega)Y_j(\omega)]$ and its inverse.

4.4.3 Initial conditions

Discrete covariance operator (without metric) In order to calculate the initial mean, modes and coefficients, one needs initial states $\chi(\omega)$ [12]from which to obtain the covariance operator.

Here, the $\chi(\omega)$ are obtained by running the old code with a small stochastic wind forcing and taking data once in 35 timesteps (one year is 36 timesteps, so that values from all seasons are obtained).

[10] Directly applying a stochastic wind stress within the programme, as done for the gyre, leads to technical difficulties due to the splitting of u and h into Kelvin- and non-Kelvin part.

[11] If v were solved for by using other oceanic quantities after the projection of these oceanic quantities, then a projection of v would not be necessary, but the ZC code solves for u, v, h simultaneously, so the only possibility is to project v, too, afterwards.

[12] these χ are not identical to the later initial realisations φ, because the realisations contain only the most dominant modes. Only in case of $N_{mode} = N_{real}$, one would have $\chi(\omega) = \varphi(\omega)$.

Since the time evolution splits u and h into u_B, h_B, A_K, one has to create initial condition for these split variables. So by χ I denote (u_B, h_B, T, A_K). In the discrete case one can consider χ as one $N \equiv (N_O + N_O + N_A + N_{XO})$ dimensional vector, where N_{XO} is the number of zonal gridpoints (A_K only depends on x) in the oceanic grid, and as before, $N_O(N_A)$ are the total number of oceanic (atmospheric) gridpoints. Letting $I = 1, 2, ...N$ denote the index of this vector, then for example χ_I with $I = 2N_O + 3N_{XA} + 5$ would be $T(i_y = 4, i_x = 5)$.

The discrete version of

$$C_{\chi(.,t_0,\omega),\chi(.,t_0,\omega)}(\mathbf{x_1}, \mathbf{x_2}) = E^\omega[\widetilde{\chi}(\mathbf{x_1}t_0, \omega) \otimes_{ab} \widetilde{\chi}(\mathbf{x_2}, t_0, \omega)]$$

is an $N \times N$ matrix with

$$C_{\chi(.,\omega),\chi(.,\omega)}(I, J) = E^\omega[\widetilde{\chi}_I(\omega)\ \widetilde{\chi}_J(\omega)] \tag{121}$$

or in matrix form $C_{\chi(.,\omega),\chi(.,\omega)} = E^\omega[\widetilde{\chi}(\omega)\ \otimes_{IJ}\ \widetilde{\chi}(\omega)]$.

Discretised 'extended' metric The metric can also be written as an 'extended' $N \times N$-matrix version. One can obtain it by rewriting eq. 120, inserting $i \to (i_x, i_y)$ where appropriate, and $u(i) = u_B(i) + A_K(i_x)\phi_K(i_y)$, $h(i) = h_B(i) + A_K(i_x)\phi_K(i_y)$:

$$\begin{aligned}
< \quad \varphi_1, \varphi_2 >= \frac{1}{N_O}\sum_{i=1}^{N_O}\{A_{uu}u_1(i)u_2(i) + A_{hh}h_1(i)h_2(i)\} \ + \ \frac{1}{N_A}\sum_{i=1}^{N_A} A_{TT}T_1(i)T_2(i) \ = \\
\frac{1}{N_O}\sum_{i=1}^{N_O}\{A_{uu}u_{B1}(i)u_{B2}(i) + A_{hh}h_{B1}(i)h_{B2}(i) \ + \ (A_{uu}u_{B1}(i) + A_{hh}h_{B1}(i))\phi_K(i_y)A_{K2}(i_x) + \\
(A_{uu}u_{B2}(i) + A_{hh}h_{B2}(i))\phi_K(i_y)A_{K1}(i_x) \ + (A_{uu} + A_{hh})\phi_K^2(i_y)A_{K1}(i_x)A_{K2}(ix)\} \ + \ \frac{1}{N_A}\sum_{i=1}^{N_A} A_{TT}T_1(i)T_2(i)
\end{aligned}$$

With φ being an N-dimensional vector, one can write the inner product as

$$< \varphi_1, \varphi_2 >= \varphi_{1,I}A^{ex}_{IJ}\varphi_{2,J}$$

(Einstein sum convention), where the $N \times N$ 'extended' metric A^{ex} can be written as block matrix

$$A^{ex} = \begin{pmatrix} A^{ex}_{uu} & 0 & 0 & A^{ex}_{uk} \\ 0 & A^{ex}_{hh} & 0 & A^{ex}_{hk} \\ 0 & 0 & A^{ex}_{TT} & 0 \\ A^{ex}_{ku} & A^{ex}_{kh} & 0 & A^{ex}_{kk} \end{pmatrix} \tag{122}$$

A^{ex}_{uu} is an $N_O \times N_O$ block with $A^{ex}_{uu}((i_x, i_y), (j_x, j_y)) = A_{uu}\delta_{i_x,j_x}\delta_{i_y,j_y}$;

A^{ex}_{hh} is an $N_O \times N_O$ block with $A^{ex}_{hh}((i_x, i_y), (j_x, j_y)) = A_{hh}\delta_{i_x,j_x}\delta_{i_y,j_y}$;

A^{ex}_{TT} is an $N_A \times N_A$ block with $A^{ex}_{TT}((i_x, i_y), (j_x, j_y)) = A_{TT}\delta_{i_x,j_x}\delta_{i_y,j_y}$;

A^{ex}_{kk} is an $N_{XO} \times N_{XO}$ block with $A^{ex}_{kk}((i_x), (j_x)) = (A_{uu} + A_{hh})\ \sum_{i_y=1}^{N_{YO}}\{\phi_K^2(i_y)\}\ \delta_{i_x,j_x}$;

A^{ex}_{uk} is an $N_O \times N_{XO}$ block with $A^{ex}_{uk}((i_x, i_y), (j_x)) = A_{uu}\phi_K(i_y)\delta_{i_x,j_x}$, similarly for A^{ex}_{hk};

and $A^{ex}_{ku} = (A^{ex}_{uk})^T$, $A^{ex}_{kh} = (A^{ex}_{hk})^T$.

Initial mean, modes, and coefficients The initial mean $\bar{\varphi}$ is simply the mean of all initial states $\chi(\omega)$.

The initial modes φ_i are the first N_{mode} eigenvectors of the metric-corrected covariance operator, $C^A_{\chi(.,\omega),\chi(.,\omega)} = C_{\chi(.,\omega),\chi(.,\omega)}A^{ex}$ or in index notation

$$C^A_{\chi(.,\omega),\chi(.,\omega)}(I, K) = C_{\chi(.,\omega),\chi(.,\omega)}(I, J)A^{ex}(J, K) = E^\omega[\widetilde{\chi}_I(\omega)\ \widetilde{\chi}_J(\omega)]A^{ex}(J, K) \tag{123}$$

This matrix is not symmetric, but it is positive semidefinite, because

$$C^A_{\chi(.,\omega),\chi(.,\omega)} = ((L^{ex})^T)^{-1}\ E^\omega[((L^{ex})^T\chi(\omega))\ \otimes_{IJ}\ ((L^{ex})^T\chi(\omega))]\,(L^{ex})^T$$

hence it formed by applying a base transformation to a mean of tensor products of two identical vectors $(L^{ex})^T\chi(\omega)$. Base transformations do not affect positive definiteness and tensor products of identical vectors are positive semidefinite, and so are their means. Hence the eigenvalues of C^A are positive (or, in some rare cases, zero).

The initial stochastic coefficients are given by $Y_i(\omega) < \chi(\omega) - \bar{\varphi}, \varphi_i >$.

With $N_{XO} = 79$, $N_{YO} = 115, N_A = 540$ C^A becomes a 18789×18789 matrix. Calculating the eigenvectors of such a matrix is rather costly (>12 hours) , so it is done only once and the initial conditions are read in for the time evolution runs.

4.5 Results

4.5.1 Initial modes and mean

The initial modes were calculated for a small ensemble of 100 realisations (fig.19-fig.21). The first mode corresponds to a well-developed El Niño. The third mode looks like a developing El Niño. Some of the lower modes show short-scale variations, especially in the velocity, which seem to merge at a point near (0^oN, 180^oE). It might be that the noise forcing used during the generation of the initial states, which is centered at this point, makes itself felt. It might be advisable to try a forcing on a larger area with lower amplitude such as not to distort the initial modes too much.

4.5.2 Simulations with the original model

Since the DO code did not run reliably in time, I tried to investigate the behaviour of ENSO in a less elegant way, namely by using the original ZC code with noise on the wind stress. As in the double gyre case, the aim is to search for coherent resonance behaviour. In order to study the simplest possible case, most of the modifications explained in 4.2.2 were used, i.e. the convergence feedback was removed and the windstress linearised, but the seasonal variability in the background was kept.

As mentioned before, there is a Hopf bifurcation in α, the parameter which couples the wind stress anomaly to the SST anomaly. So the original code was run without noise, and with white and red noise, for various valus of α. The dimensionless value used by Cane and Zebiak is $\alpha = 1.6$, which corresponds to $0.031\, m^2 s^{-3} K^{-1}$; at this value, the model keeps creating El Niños after an initial spin-up, i.e. it is past the Hopf. Hence values of α between 1.0 and 1.6 were used.

The stochastic noise was given a Gaussian shape centered at $(0^oN, 180^oE)$ within ($6^oS - 6^oN$, $163.125^oE - 163.125^oW$) and zero outside this domain. The noise amplitudes chosen are 0.5, 1.5 and $4.5\, dy/cm^2$. The coherence time is either zero (white noise) or $0.5\, years$ - this is still significantly shorter than El Niño's timescale but longer than most atmospheric variability (Madden-Julian oscillation: 1-3 months). After a spin-up of 60 years (with a short windburst in the first months in case of zero noise) a time series of 200 years with one measurement per month is generated for each parameter setting.

As a measure for the 'El Niño activity' of the system under certain parameters the variance (in time) of the mean temperature in the Nino3 index area ($6^oS - 6^oN$, $151.75^oW - 95.5^oW$) was used; in order to filter out seasonal effects, the data of each month was treated seperately. A plot of the variance is given in fig. 22 for the months march, june, september and december. The results are very similar for all months.

For $\alpha \leq 1.2$ and zero noise, the variance is very small, while between 1.4 and 1.6 the increase is only moderate. Apparently the Hopf bifurcation is located somewhere near $\alpha = 1.3$.

In the presence of noise, the variance at small α is several orders of magnitudes larger than without noise, while for $\alpha \geq 1.4$ the noise has no influence anymore. So before the Hopf bifurcation the system is excited by noise, whereas after the Hopf, the internal oscillations is so large that the noise forcing becomes negligible. It can be clearly seen from the figure that for small α the variance increases with the noise amplitude, and also that red noise produces higher variances than white noise with the same amplitude.

In order to check whether the observed variance is really due to El Niño, the dominant five eof's in the variables T, u, v,h were calculated on the atmospheric grid (the atmospheric grid is coarser, so the calculation of the eigenfunctions is done in minutes rather than hours). In fig. 23-25 the temperature field of the december eof's is plotted, for $\alpha = 1.2$ (before the Hopf) and zero, white and red noise with amplitude 4.5.

In absence of noise, there is no organised pattern in the temperature field. For white noise, the first mode shows a temperatur anomaly along the equator, i.e. it is El Niño-like. For red noise, the pattern becomes even clearer. The asymmetry around the equator near the coast is due to the asymmetric background upwelling. The rather localised patch in the western part of the basin is an artefact of the rather localised noise. The very small magnitudes of the temperatures in the modes is due to the fact that the eof's were calculated with the variables T, u, v,h , and the

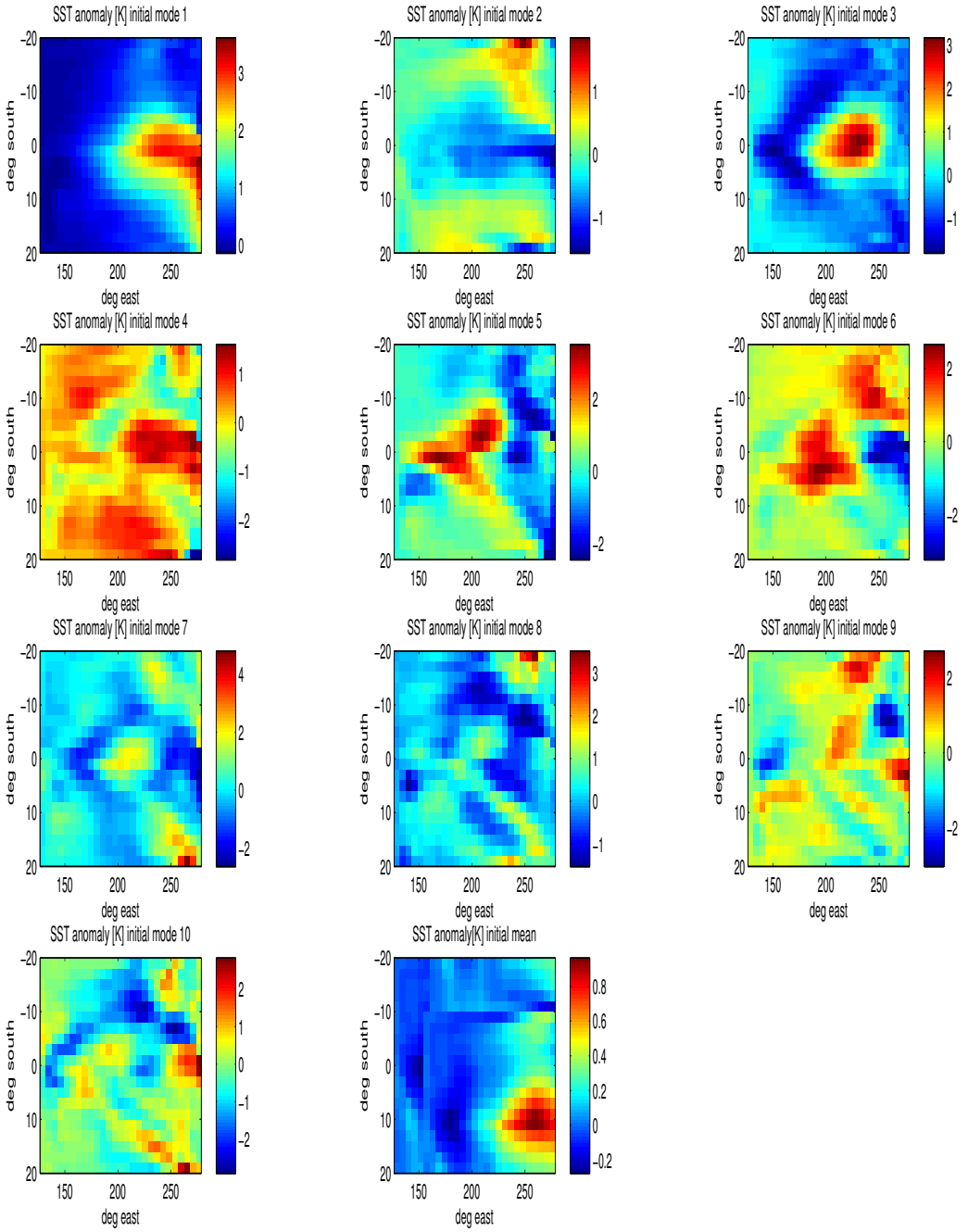

Figure 19: SST anomaly field of the initial modes (first 10 panels) and mean (bottom middle).

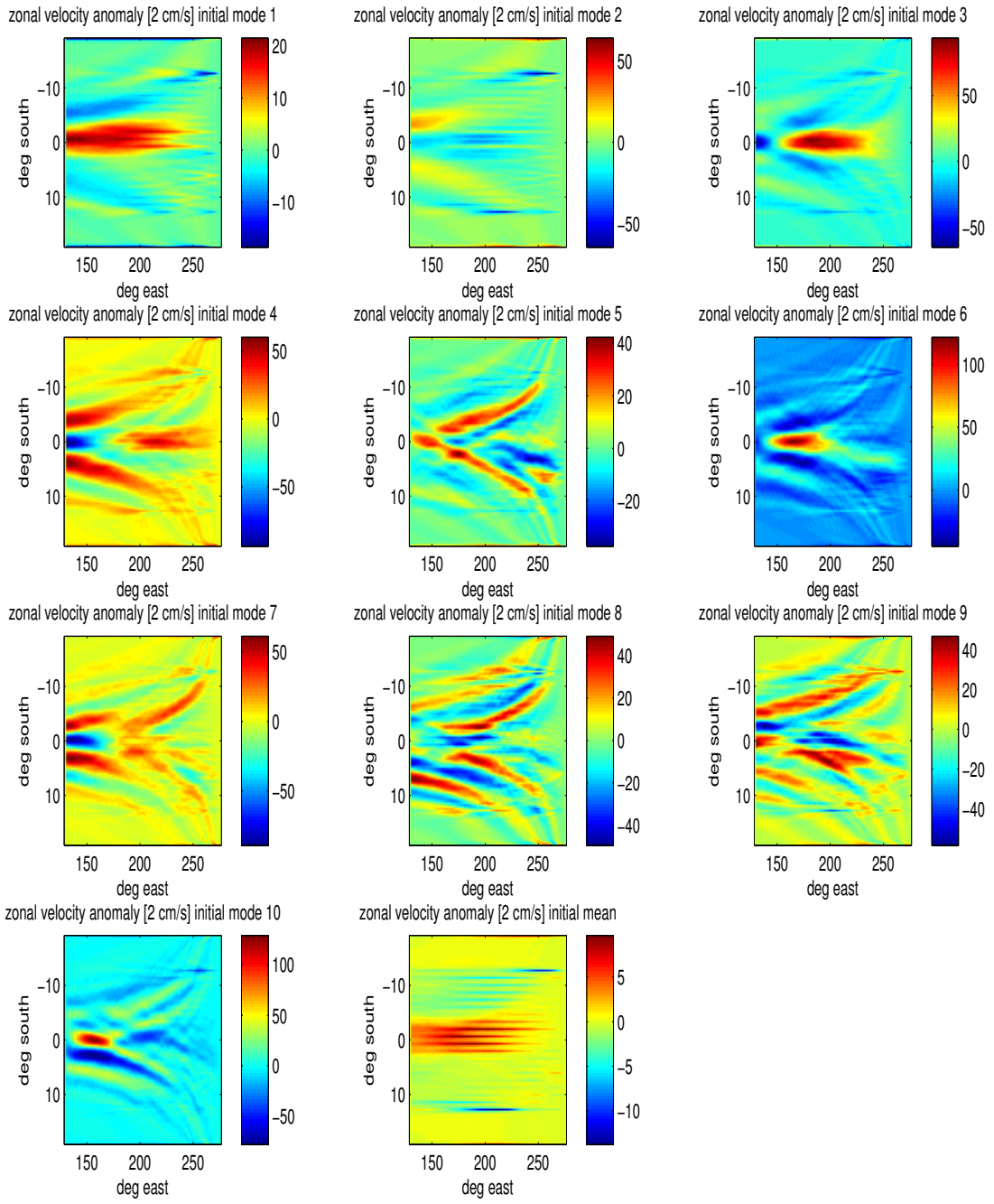

Figure 20: Total (Kelvin+non-Kelvin) zonal velocity anomaly field of the initial modes (first 10 panels) and mean (bottom middle).

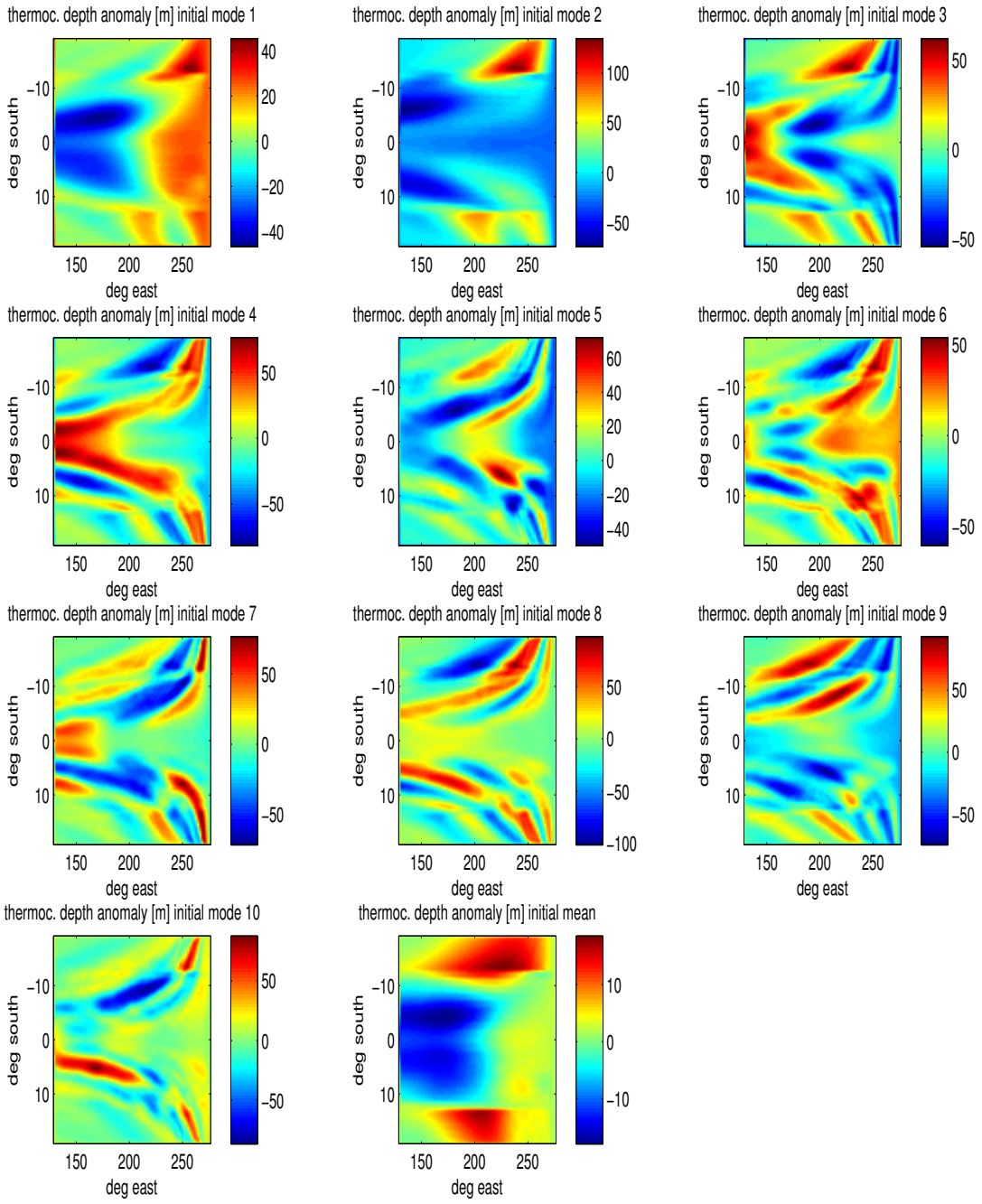

Figure 21: Total (Kelvin+non-Kelvin) thermocline depth anomaly field of the initial modes (first 10 panels) and mean (bottom middle).

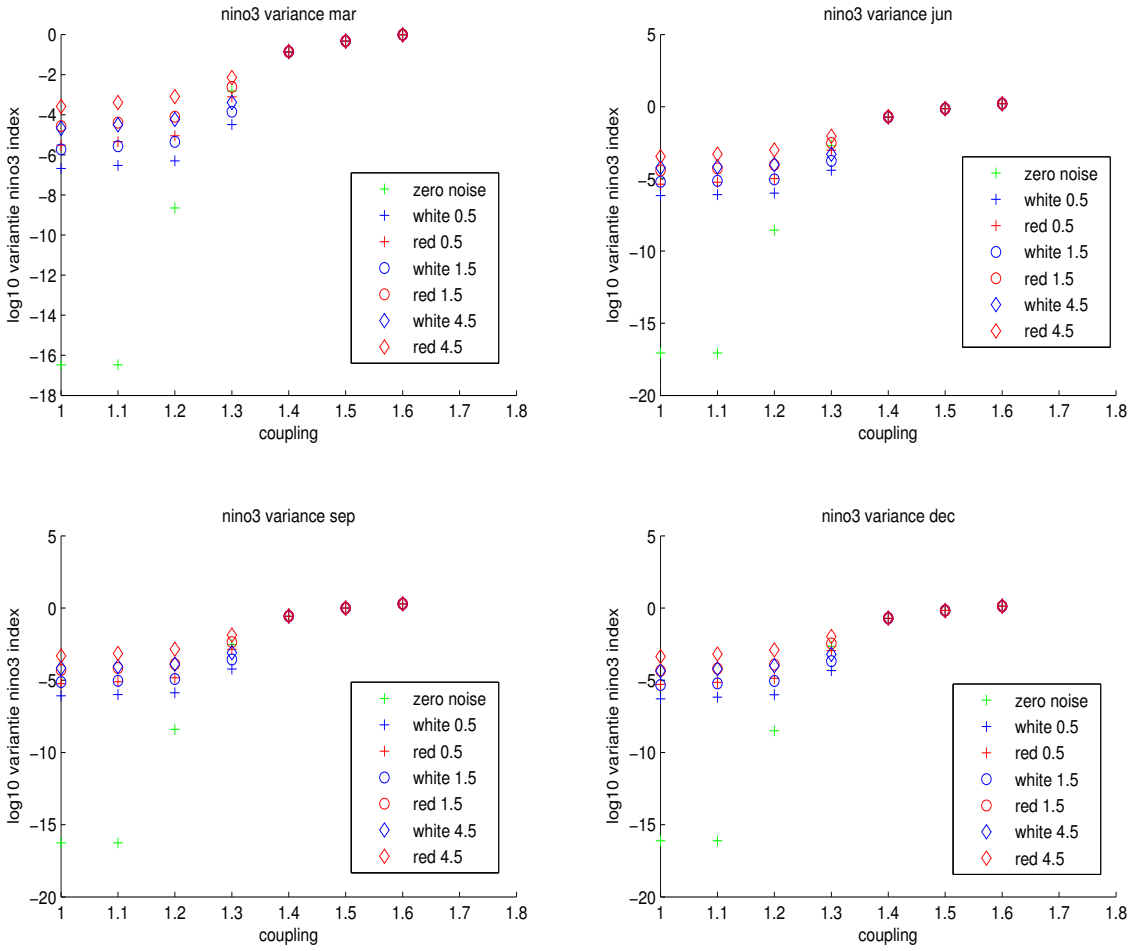

Figure 22: Variance of the SST in the Nino3 area against the heating parameter α for different noise types (green: no noise, blue: white noise, amplitude 0.5, 1.5, 4.5 , red: red noise with decorrelation time of 6 months, same amplitudes), for the months march, june, september, december.

velocities and thermocline height take larger numerical values that the temperature. Since the eof's are normalised to 1, the temperature values become very small. (This does not happen for the initial modes because metric.)

The experiment with the original code suggests that El Niño indeed has a coherence resonance behaviour: The El Niño-like Hopf mode which is not active for small heating parameter without noise can be excited by noise, where red noise works better than white noise.

5 Summary and Outlook

The DO method provides an efficient tool to deal with stochastic differential equations which one obtains when dealing with noise. Not only does it give insight into the effect of the noise, but it also reveals much of the dynamics of the system - one can obtain modes linked to certain processes for which one was not searching explicitely. (On the other hand, it does not provide an explanation/interpretation of the modes, so that additional knowledge or research is needed for understanding the underlying processes.)

The experiments done with the Double Gyre code nicely illustrate this. For the range of Reynolds numbers covered, one finds both the pitchfork mode, which is linked to the bimodality of the Kuroshio current, and two transient responses, namely the Gyre mode, which has a period of about 1 year (3 years for larger basins) and is associated to the second Hopf bifurcation, and the Rossby basin mode, with a 2monthly (7 monthly) period, which is associated to

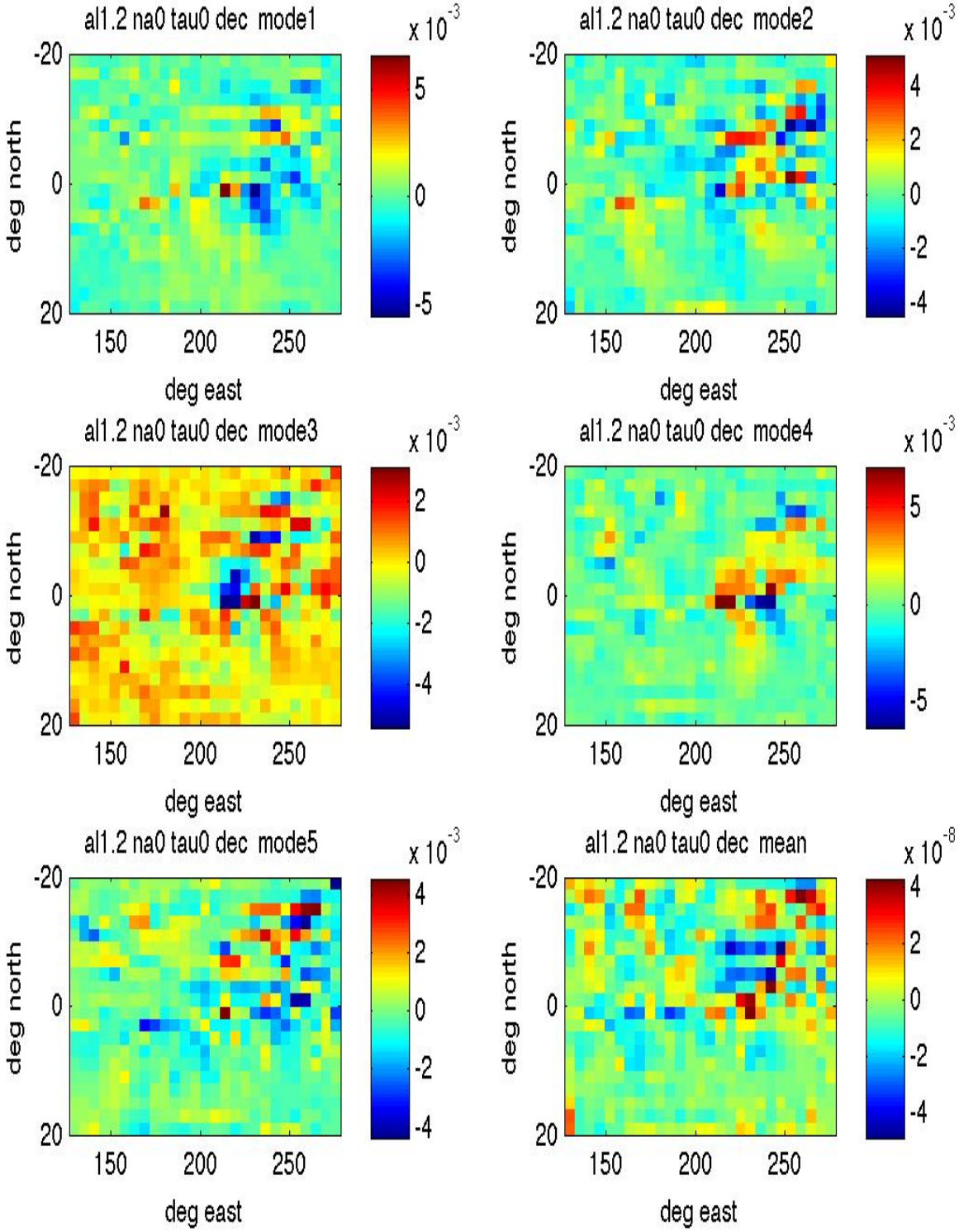

Figure 23: Temperature field of the 5 dominant EOF's and the mean (bottom right), calculated from the runs of the original ZC code with zero noise for the month december and heating parameter $\alpha = 1.2$.

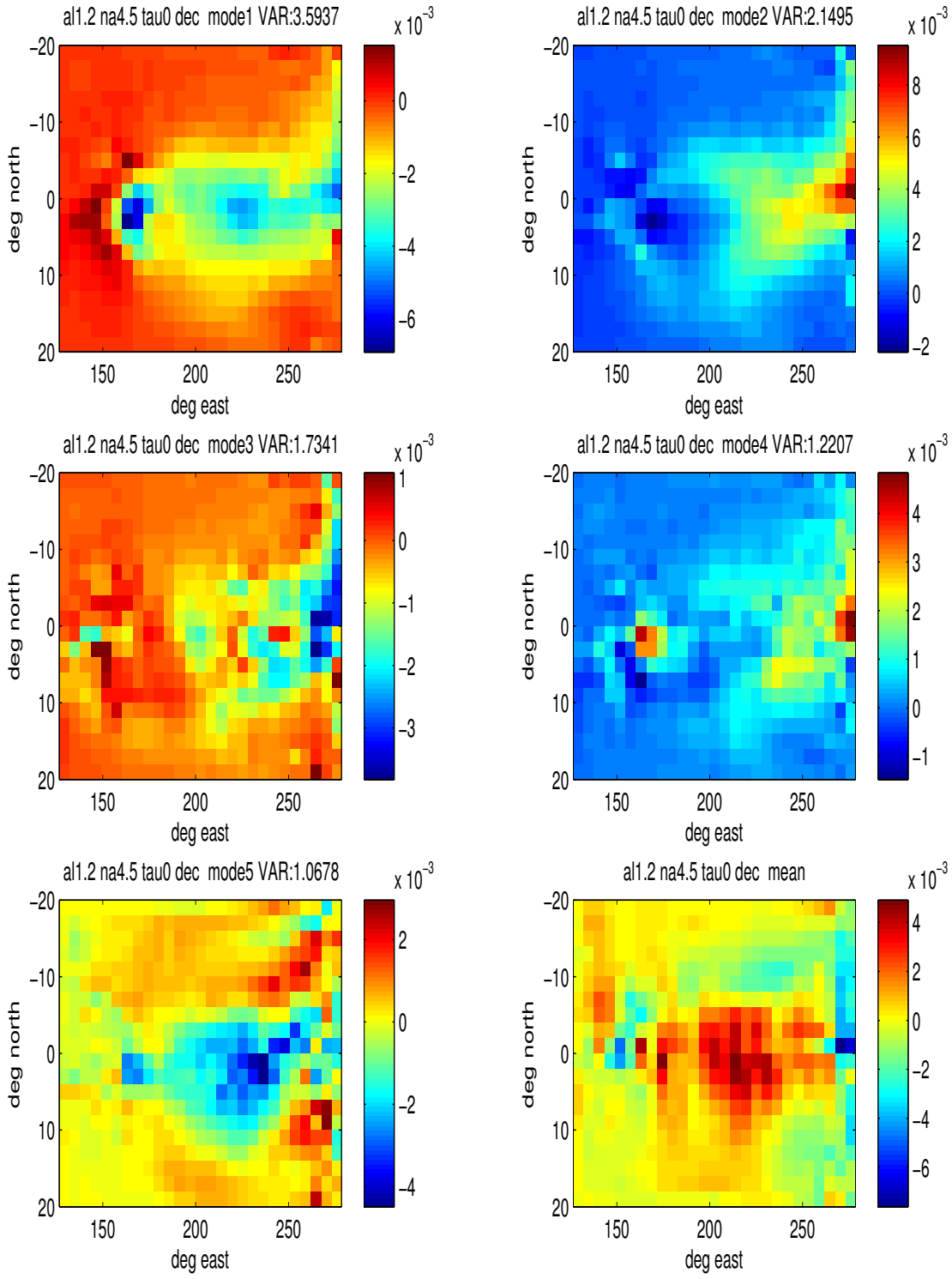

Figure 24: Temperature field of the 5 dominant EOF's and the mean (bottom right), calculated from the runs of the original ZC code with white noise (amplitude $4.5 dyn/cm^2$) for the month december and heating parameter $\alpha = 1.2$.

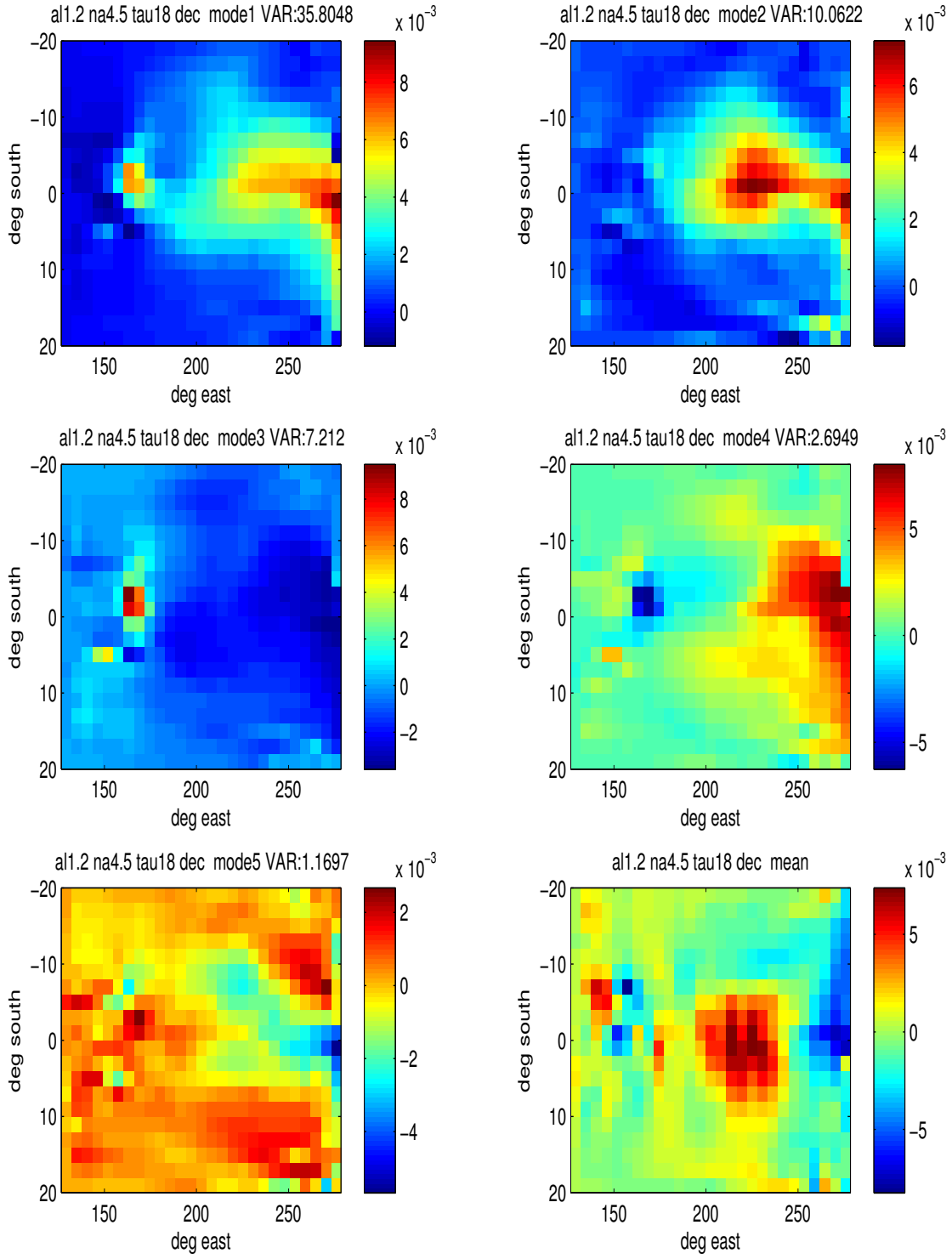

Figure 25: Temperature field of the 5 dominant EOF's and the mean (bottom right), calculated from the runs of the original ZC code with red noise ($\tau = 6 months$, amplitude $4.5 dyn/cm^2$) for the month december and heating parameter $\alpha = 1.2$.

the first Hopf bifurcation. Interestingly, the gyre mode is more easily excited even at low Reynolds number than the Rossby basin mode. For the latter it was tried to show that it has coherent resonance behaviour. Indeed, it is more easily excited by red noise than by white noise at low Re, and occurs even without noise (excitation during spinup) close to the Hopf bifurcation. However, the data is not sufficient to claim with certainty that coherence resonance behaviour has been found; in addition, some significance tests are necessary in order to be confident that the peaks in the Fourier spectra are really physical.

Probably due to the rather low temporal and spatial resolution, run the model had to be run with a rather low noise amlitude. This might explain the decay of the variance after the spinup, even in the preence of noise. It would be interesting to repeat the experiment at higher resolution and noise amplitude.

An interesting observation is the 'synchronisation' of the stochastic coefficients, which might be caused, or enhanced, by the realisation-independent noise. It might also reduce the variance through energy transfer to the mean. One might inverstigate this further by calculating the energy transfer between the modes and the mean, as is done in [Sapsis, Dijkstra 2013], and by performing simulations with a realisation-depenent forcing.

For El Niño, the DO equations were derived. It was shown that taking the limit of a vanishing time derivative after applying DO is equivalent to treating that equation as a diagnostic constraint from the start, provided that the corresponding metric components vanish. This is indeed what happens for the Zebiak-Cane model when applying the long-wave limit to the meridional momentum equation. It was also necessary to find a sensible expression for the thermal contribution to the metric, and it turned out that for a non-trivial metric A, the initial modes cannot be taken to be the eigenvecotrs of the covariance matrix C, but of CA.

Due to lack of time, the next step, namely implementing the DO formalism into a deterministic code of the Zebiak-Cane model, was not finished. However, a preliminary study with the original code suggests that El Niño has coherence resonance behaviour for the Hopf bifurcation in the heating parameter. I have hope that my code will run properly in a couple of weeks, so that I can verify and extend these preliminary results using the DO method.

References

[Dijkstra 2005] Dijkstra, Nonlinear Physical Oceanography, Springer, 2005

[Dijkstra 2010] Dijkstra, Dynamical Oeanography, Springer, 2010

[Dijkstra,Katsman 1997] Dijkstra, Katsman, Temporal variability of the wind-driven quasigeostrophic double gyre ocean circulation: Basic bifurcation diagrams. Geophys.Astrophys. Fluid Dyn., 1997

[Schmeits, Dijkstra 2002] Schmeits, Dijkstra, Subannual variability of the ocean circulation in the Kuroshio region, Journal of geophysical research, 2002

[Schmeits, Dijkstra 2001] Schmeits, Dijkstra, Bimodality of the Kuroshio and the Gulf Stream, Journal Phys. Oceanogr., 2001

[Simmonet, Dijkstra 2002] Simonnet, Dijkstra, Spontaneous generation of low-frequency modes of variability in the wind-driven ocean circulation, J.Phys.Oceanogr., 2002

[Dijkstra, Burgers 2002] Dijkstra, Burgers, Fluid dynamics of El Niño variability, Annu. Rev. Fluid Mech., 2002

[Kleeman 2010] Kleeman, R. Stochastic theories for the irregularity of ENSO, Royal Society Publishing, 2010

[Zebiak, Cane 1987] Zebiak, Cane, A model El Niño - Southern Oscillation, monthly weather review, 1987

[Sapsis, Lermusiaux 2009] Sapsis, Lermusiaux, Dynamically orthogonal field equations for continuous stochastic dynamical systems, Physica D 238, 2009

[Sapsis, Dijkstra 2013] Dijkstra, Sapsis, Interaction of Additive Noise and Nonlinear Dynamics in the Double-Gyre Wind-Driven Ocean Circulation, Journal Phys. Oceanogr., 2013